



## Modeling and simulation of large-scale ductile fracture in plates and shells

Bo Ren<sup>a,b</sup>, Shaofan Li<sup>a,c,\*</sup>

<sup>a</sup> Department of Civil and Environmental Engineering, University of California, Berkeley, CA 94720, USA

<sup>b</sup> School of Hydro-power and Information Engineering, Huazhong University of Science and Technology, Wuhan 430074, China

<sup>c</sup> School of Civil Engineering and Mechanics, Huazhong University of Science and Technology, Wuhan 430074, China

### ARTICLE INFO

#### Article history:

Received 7 January 2012

Received in revised form 22 April 2012

Available online 9 May 2012

#### Keywords:

Ductile fracture

Crack propagation

Gurson model

Johnson–Cook model

Meshfree method

Plates and shells

### ABSTRACT

The work is concerned with the modeling and simulation of large scale ductile fracture in plate and shell structures. A meshfree method – the reproducing kernel particle method (RKPM) – is used in numerical computations in order to enact dynamic crack propagation without remeshing. There are several novelties in the present approach. First, we have developed a crack surface approximation and particle split algorithm for three-dimensional through-thickness cracks. Second, to represent evolving crack surface in 3D shell structures, a 3D parametric visibility condition algorithm is proposed, which re-constructs the local connectivity map for particles near the crack tip or crack surfaces, so that the meshfree interpolation field can represent physical material separation in the computational domain. Third, the constitutive update formulas in explicit time integration by different versions of Gurson models and the rate-dependent Johnson–Cook model are implemented for 3D computations. Finally, the performance of different Gurson-type models are investigated and compared with the experimental data of large scale in-plate tear process. Numerical simulations of crack propagation in stiffened plates and shells demonstrate that the proposed method provides an effective means to simulate ductile fracture in large scale plate/shell structures with engineering accuracy.

© 2012 Elsevier Ltd. All rights reserved.

### 1. Introduction

The crack propagation in metallic and composite plate and shell structures is a common failure phenomenon encountered in engineering structures such as in ship grounding, aircraft fuselage rupture, and automobile vehicle crash, etc. There have been many experimental studies reported in the literature about dynamic fracture process in large scale engineering structures. For instance, Erdogan and Ratwani (1972) conducted a both experimental and analytical study of fracture of cylindrical and spherical shell structures; Simonsen and Tornqvist (2004) investigated the in-plate tear and tension fracture of a large scale plate in experiments as well as in numerical simulations; and Alsos and Amdahl (2009) and Alsos et al. (2009) also studied ductile fracture or puncture of stiffened plates by carrying out hull indentation tests on the plates.

In current computational engineering practice, there are essentially three approaches to simulate fracture by adjusting the topology structure of a FEM mesh in order to represent a ongoing material surface separation in the computational domain: (1) use the so-called element erosion technique, e.g. Chen (1992), to create a region separation, which simply discards or ‘kills’ the elements along the crack path; (2) embed cohesive zone (crack) paths in the

original FEM mesh e.g. Tvergaard and Hutchinson (1996) and Tvergaard (2001), which will allow crack propagating along the cohesive zone network, and (3) adding appropriate discontinuous functions as an enrichment to represent surface separation, which is known as the so-called eXtended finite element method (X-FEM) (Moës et al., 1999; Bordas et al., 2008). The first approach has been extensively used and implemented in commercial FEM softwares, which leads to loss of the element mass, energy, momentum, and results the loss of overall accuracy theoretically. However, in practice, it can be made fairly accurate by using a constitutive model that couples with a damage indicator, such as the Gurson model (Gurson, 1977). Here the load carrying capacity of the removed elements can be made close to zero with a proper criterion. The second approach is a phenomenological model, and it is proven difficult to construct proper cohesive laws for 3D ductile material under mixed load condition. The third approach is mainly applicable to brittle or quasi-brittle fractures. On the other hand, ductile failure, especially large scale ductile fracture, is often associated with large scale yielding, finite plastic deformation, as well as temperature rise. These often occur during high strain rate loadings with localized high strain gradients, which usually accompanies with severe mesh distortion. In general, the mesh based approach may have difficulties to simulate history dependent ductile fracture process.

Meshfree or particle-based methods (e.g. Li and Liu (2004)) have intrinsic advantages to represent evolving geometry of the computational domain during crack propagation. To solve

\* Corresponding author at: Department of Civil and Environmental Engineering, University of California, Berkeley, CA 94720, USA.

E-mail addresses: [boren@berkeley.edu](mailto:boren@berkeley.edu) (B. Ren), [shaofan@berkeley.edu](mailto:shaofan@berkeley.edu) (S. Li).

engineering fracture problems, Belytschko and his co-workers (e.g. Belytschko et al. (1995)) have developed the Element Free Galerkin (EFG) method to simulate crack growth; Liu et al. (1999) demonstrated the ability of RPKM for large deformation fracture and damage problems, and Li and Simonsen (2005) proposed a 2D parametric crack formation algorithm to update meshfree interpolation field to represent the evolving crack automatically. Based on this algorithm, Simkins and Li (2006) incorporated the thermal effect into ductile failure process; Rabczuk and Areias (2000) have used meshfree method to simulate elastic fracture in thin shell structures, and Qian et al. (2008) have employed RKPM method to simulate ductile fracture in thin shell structures. Recently, Rabczuk and his co-workers (Rabczuk and Zi, 2007; Rabczuk et al., 2007; Rabczuk et al., 2008) have combined meshfree particle method with extended finite element method (X-FEM) to develop a class of extended meshfree method to simulate cohesive fracture. Ren and Li (2010) proposed a meshfree algorithm to represent crack nucleation, growth, and arrest automatically to simulate two-dimensional plugging fracture problems. Recently, Ren et al. (2011a) reported their effort to develop a two-dimensional meshfree void growth algorithm that can be used for spall fracture simulation as well.

There are two main challenges in simulating ductile fracture in 3D engineering plate/shell structures. First, the evolving crack surface leads to time-evolving traction-free boundary growth in computational domain, hence the finite element representation of evolving material geometry and topology have to change accordingly. To do so without remeshing and computational unloading is a real challenge in 3D ductile fracture simulations. This is because ductile fracture is a thermodynamic irreversible process, the loading and unloading processes, no matter they are physical or computational, are path-dependent and dissipative. Second, the large scale ductile fracture often undergoes drastic plastic deformation, which makes ductile fracture a multi-scale problem (Antoun et al., 2003). How to predict macro-scale mechanical behavior of structures with micro-scale damage feature is the other challenge.

In the recent decades, there have been many works reported in the literature studying how to predict ductile fracture, e.g. finite element approach (FEA) by Anderson (1995) and Mikkelsen (1997), and meshfree approach by Li and Simonsen (2005), Ren and Li (2010) and Ren et al. (2011a,b). However most of these efforts remain as academic research that is mainly demonstrated by 2D illustration problems. Recently researchers have applied different numerical methods simulating fractures in engineering structures e.g. using the cohesive zone model by Cirak et al. (2005) and using X-FEM method by Song and Belytschko (2009). However, most of these works are still focused on fractures in brittle materials.

To predict material failure behavior, a successful approach is to employ linear elastic fracture mechanics theory (LEFM), which uses J-integral or stress intensity factor to evaluate material toughness in predicting material failure. LEFM gives satisfactory description of crack tip fields for brittle fracture or fracture under small scale yielding. However LEFM is unable to predict ductile fracture process especially for large scale yield and drastic finite plastic deformation (Anderson, 1995). The ductile failure may be interpreted as a process of voids nucleation-growth-coalescence (Chevrier and Klepaczko, 1999). Voids are nucleated at the sites of inhomogeneity or inclusion inside solids at mesoscale, and they may then grow and coalesce. Some void growth can be triggered by local deformation, for instance by the triaxial deformation or triaxial strain rate. During void coalescence, voids merge with each other, and macro-scale cracks start to form (Antoun et al., 2003).

Lacking energy release indicator around the ductile crack tip, alternative approaches have been developed for ductile fracture such as micromechanics-based damage approach, which models the ductile failure at constitutive modeling stage with an evolving

material damage measure at the fine scale. Well-known examples are the Rice–Tracey model (Rice and Tracey, 1969) and the Johnson–Cook model (Johnson and Cook, 1985), where the accumulative damage indicator is related to plastic strain, void population, or triaxial stress, etc. Once a macro-scale damage indicator reaches certain threshold, a macro-scale crack may start to grow. Based on multi-scale micromechanics, Gurson (1977) derived an inelastic damage model that governs macro-scale plastic flow, in which the damage indicator is related to the micro-scale void volume fraction, i.e., the ratio of voids volume in a Representative Volume Element (RVE), and it is incorporated into the macro-scale material constitutive law. Consequently, the Gurson model relates the macro fracture behavior to micro-scale damage evolution.

The original Gurson model was formulated and calibrated based on the mechanics of void growth under axisymmetric stress state (Gurson, 1977; Nahshon and Hutchinson, 2008). Tvergaard and Needleman (1984) made the Gurson model into a computational model, and introduced a physics-based computation algorithm to model void nucleation, growth and coalescence; their model is now commonly referred to as the Gurson–Tvergaard–Needleman model (GTN model). Recently, by considering the damage mechanisms such as void distortion and inter-void interaction under purely shear deformation state, Nahshon and Hutchinson (2008) modified the mechanism of void fraction growth by taking into account the effect of shear stress. Their model is referred as the Shear Modified Gurson (SM-Gurson) model in this paper. However, as pointed out by Nielsen and Tvergaard (2009), the additional damage contribution from SM-Gurson model may be over-estimated when stress triaxiality is high. To remedy this shortcoming, Nielsen and Tvergaard (2010) make the shear stress contribution depending on the level of stress triaxiality, and we refer their model as the Modified Gurson (M-Gurson) model in this paper. The M-Gurson model is considered to be able to capture mixed-mode fracture behavior.

Ductile fracture is often accompanied with enormous high plastic deformation, and in turn the material plastic flow will generate a large amount of heat at the local area where material exhibits viscoplastic behavior. However, the various Gurson models mentioned above are still rate-independent plasticity model, and they do not consider thermo-mechanical coupling effect. To take into account the rate-dependent and thermal-mechanical coupling effects, Johnson and Cook (1983, 1985) proposed a rate-dependent plasticity constitutive model, which is referred to as the Johnson–Cook model.

The scope of the paper is focused on discussion of meshfree computational formulation and algorithm to simulate large scale ductile fracture in engineering plate/shell structures. The paper is organized in seven sections. In Section 2, the Galerkin weak formulas and interpolation function of 3D RKPM method are discussed. In Section 3 the crack surface approximation and a 3D parametric visibility condition algorithm are discussed. In Section 4, the different versions of Gurson-type models and the related constitutive update are discussed. In Section 5, we briefly introduce the Johnson–Cook model and its constitutive update; and in Section 6 the results of numerical simulations are reported to validate and demonstrate the capacity of the proposed method. Finally, to conclude the work, a few remarks are made in Section 7.

## 2. Modeling and meshfree discretization

### 2.1. The nonlinear kinematics

Usually the fracture in metallic material goes with dramatic plastic deformation. To solve this nonlinear problem, we first describe some basic kinematic definitions that will be later used in

the constitutive update. In meshfree simulations, a particle  $\mathbf{X}$  in reference configuration at  $t = 0$ , will move to  $\mathbf{x}$  in the current configuration at time  $t$ . The deformation gradient is then defined as:

$$\mathbf{F} = \frac{\partial \mathbf{x}}{\partial \mathbf{X}} = x_{ij} \mathbf{e}_i \otimes \mathbf{E}_j \quad (1)$$

where  $\mathbf{e}_i$  and  $\mathbf{E}_j$  denote the coordinate basis vectors in reference and current configurations respectively. The determinant of  $\mathbf{F}$  is denoted as  $J = \det|\mathbf{F}|$ .

In this work, a total Lagrange approach is adopted to represent finite deformation of solids.

The rate of deformation and the rate of spin can be expressed as:

$$\mathbf{d} = (\dot{\mathbf{F}} \cdot \mathbf{F}^{-1} + \mathbf{F}^{-T} \cdot \dot{\mathbf{F}}^T) / 2 \quad (2)$$

$$\mathbf{w} = (\dot{\mathbf{F}} \cdot \mathbf{F}^{-1} - \mathbf{F}^{-T} \cdot \dot{\mathbf{F}}^T) / 2 \quad (3)$$

where  $\dot{\mathbf{F}} = \frac{\partial \dot{\mathbf{x}}}{\partial \mathbf{X}}$ .

For ductile fracture problems, the total rate of deformation can be decomposed to elastic, plastic, and thermal parts,

$$\mathbf{d} = \mathbf{d}^e + \mathbf{d}^p + \mathbf{d}^t \quad (4)$$

### 2.2. Galerkin variational weak formulation

The equation of balance of linear momentum for a continuum in a computational domain at reference configuration  $\Omega_0$  is,

$$\nabla_{\mathbf{x}} \mathbf{P} + \rho_0 \mathbf{b} = \rho_0 \ddot{\mathbf{u}} \quad (5)$$

where  $\mathbf{P}$  is the first Piola–Kirchhoff stress, which is related to the Cauchy stress as  $\mathbf{P} = J \boldsymbol{\sigma} \cdot \mathbf{F}^{-T}$ ;  $\mathbf{b}$  denotes the body force,  $\rho_0$  is the initial density of material, and  $\mathbf{u}$  is the displacement field.

The Galerkin weak formulation of (5) can be written as,

$$\int_{\Omega_0} \mathbf{P} : \delta \mathbf{F} d\Omega_0 - \int_{\Gamma_0^T} \mathbf{T} \cdot \delta \mathbf{u} dS - \int_{\Omega_0} \rho_0 \mathbf{b} \cdot \delta \mathbf{u} d\Omega_0 + \int_{\Omega_0} \rho_0 \ddot{\mathbf{u}} \cdot \delta \mathbf{u} d\Omega_0 = 0 \quad (6)$$

where  $\delta \mathbf{u}$  is the test function,  $\Gamma_0^T$  denotes the traction boundary where traction  $\mathbf{T}$  is prescribed. For meshfree simulations, the test function  $\delta \mathbf{u}$  does not automatically satisfy the essential boundary condition, therefore some special care must be taken to handle essential boundary condition (see Li and Liu (2004)).

For the Galerkin type weak form solutions such as FEM and meshfree method, the field variable is represented by values of nodal points over a generally complex domain  $\Omega_0$ , and the interpolation function is used to approximate the field variable, such as position vector  $\mathbf{u}(t)$ , at any time instance  $t$ ,

$$\mathbf{u}(\mathbf{X}, t) = \sum_I N_I(\mathbf{X}) \mathbf{u}_I(t) \quad (7)$$

where  $N_I$  denotes the global interpolation shape function, and we shall discuss a meshfree interpolation function (RKPM) in next section.  $\mathbf{u}_I$  is the nodal displacement. Considering the Bubnov–Galerkin method, the test function  $\delta \mathbf{u}$  is constructed using the same shape function as that of the trial function  $\mathbf{u}$ , consequently we can obtain,

$$\delta \mathbf{u}(\mathbf{X}, t) = \sum_I N_I(\mathbf{X}) \delta \mathbf{u}_I(t) \quad (8)$$

Substituting Eqs. (7) and (8) into the weak form Eq. (6), we can derive the discrete dynamic equation,

$$[\mathbf{M}] \ddot{\mathbf{u}} + \mathbf{f}^{int} - \mathbf{f}^{ext} = 0 \quad (9)$$

where  $\mathbf{f}^{int}$  and  $\mathbf{f}^{ext}$  are internal and external nodal force vectors respectively, and  $\mathbf{M}$  is the mass matrix, which is then simplified by using the row-sum lumped mass matrix. The components of internal force, external force, and the mass matrix are given as,

$$f_{ii}^{int} = \int_{\Omega_0} P_{ij} \partial N_i / \partial X_j d\Omega_0, \quad (10)$$

$$f_{ii}^{ext} = \int_{\Omega_0} \rho_0 b_i N_i d\Omega_0 + \int_{\Gamma_0^T} T_i N_i dS \quad (11)$$

$$M_{IJ} = \int_{\Omega_0} \rho_0 N_I \delta_{IJ} d\Omega_0, \quad (12)$$

in which the row-sum lumped technique is used in computing the mass matrix.

### 2.3. RKPM meshfree approximation

In Eq. (7), the interpolation shape function  $N_I(\mathbf{X})$  is introduced, which depends on the adopted approximation method. In this work, we employ a meshfree method – the reproducing kernel particle method (RKPM) – to simulate ductile fracture. The RKPM meshfree shape function  $N_I(\mathbf{X})$  may be viewed as an enhanced version of original Smoothed Particle Hydrodynamics (SPH) shape function (Lucy, 1977). The basic ideal of RKPM is to construct a proper kernel function by ‘correcting’ the original SPH kernel function,  $w(\mathbf{X}, \mathbf{X}_I)$ , to satisfy the partition of unity condition and reproduce linear functions so that the rigid body motion and uniform deformation can be correctly represented. The RKPM interpolation function can be written as (Li and Liu, 2004):

$$N_I(\mathbf{X}) = C(\mathbf{X}, \mathbf{X}_I) w(\mathbf{X}, \mathbf{X}_I) \Delta \Omega_{0I} \quad (13)$$

In this work,  $w(\mathbf{X}, \mathbf{X}_I)$  is obtained by a Cartesian product of the one-dimensional cubic spline function,  $\Delta \Omega_{0I}$  is the volume that particle  $I$  possesses, and  $C(\mathbf{X}, \mathbf{X}_I)$  is the so-called correction function:

$$C(\mathbf{X}, \mathbf{X}_I) = \mathbf{B}^T(\mathbf{X}) \mathbf{p}(\mathbf{X}, \mathbf{X}_I) \quad (14)$$

It should be noted that the correction function ensures the accuracy of RKPM interpolation function in order to solve displacement field at any point, for example at a crack tip. In above equation,  $\mathbf{p}(\mathbf{X}, \mathbf{X}_I)$  is the interpolation basis function:

$$\begin{aligned} \mathbf{p}^T(\mathbf{X}, \mathbf{X}_I) = & [1, X_1 - X_{I1}, X_2 - X_{I2}, X_3 - X_{I3}, (X_1 - X_{I1})(X_2 - X_{I2}), \\ & (X_2 - X_{I2})(X_3 - X_{I3}), (X_1 - X_{I1})(X_3 - X_{I3}), \\ & (X_1 - X_{I1})(X_2 - X_{I2})(X_3 - X_{I3})] \end{aligned} \quad (15)$$

In Eq. (14),  $\mathbf{B}(\mathbf{X})$  is a coefficient vector, and it is determined by the reproducing condition (Li and Liu, 2004), which is given as following,

$$\mathbf{B}(\mathbf{X}) = \mathbf{m}^{-1}(\mathbf{X}) \mathbf{p}(0) \quad (16)$$

$$\mathbf{m}(\mathbf{X}) = \mathbf{p}(\mathbf{X}, \mathbf{X}_I) \mathbf{p}^T(\mathbf{X}, \mathbf{X}_I) w(\mathbf{X}, \mathbf{X}_I) \Delta \Omega_{0I} \quad (17)$$

$$\mathbf{p}^T(0) = (1, 0, 0, 0, 0, 0, 0, 0) \quad (18)$$

Assume that there is a valid particle distribution with total  $n_p$  particles, and they are position initially in the reference configuration,  $\mathbf{X}_I \in \Omega_0$ ,  $I = 1, \dots, n_p$ . The RKPM interpolation field, for instance for the displacement field, can be expressed as,

$$\mathbf{u}^h(\mathbf{X}, t) = \sum_{I=1}^{n_p} N_I(\mathbf{X}) \mathbf{u}_I(t) \quad (19)$$

where  $N_I(\mathbf{X})$  is the RKPM shape function.

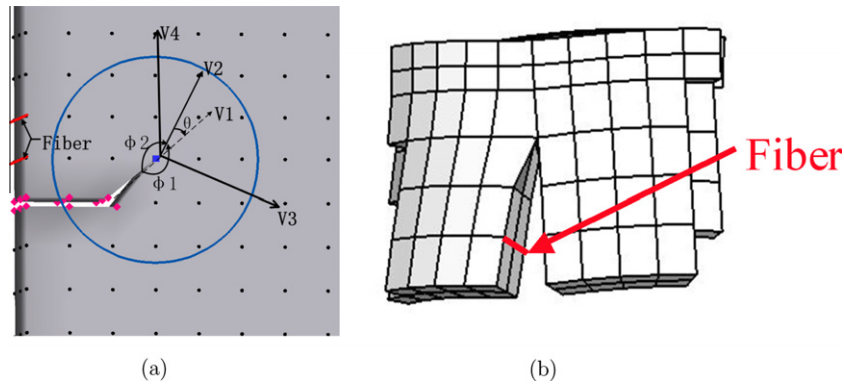


Fig. 1. Crack approximation in large scale plate, (a) crack tip searching algorithm, (b) illustration of fiber.

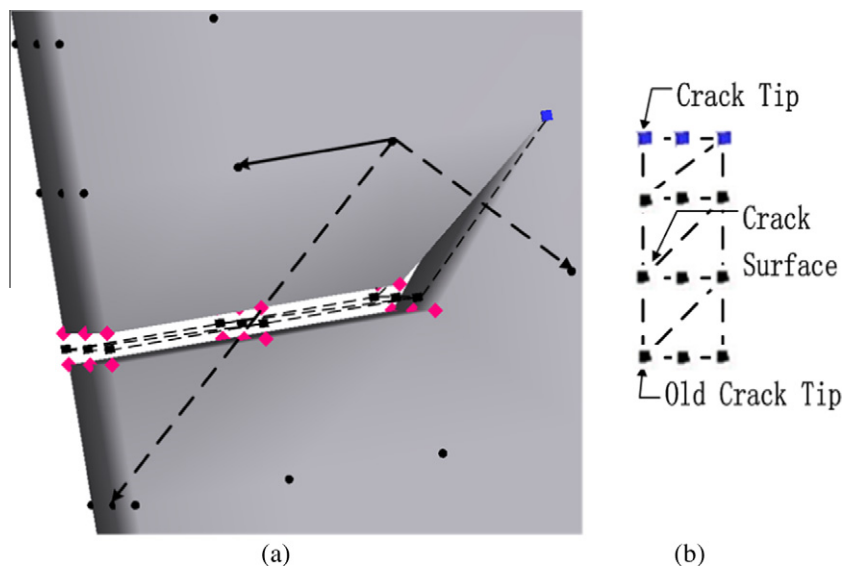


Fig. 2. Crack approximation in 3D plate, (a) particle splitting around crack tip, (b) 2D illustration of crack surface approximation.

### 3. 3D visibility condition and 3D crack growth algorithm

#### 3.1. Crack approximation in plate structures

From computational viewpoint, crack propagation may be viewed as the growth of traction-free boundary in the computational domain, and it is associated with evolving and changing of the interpolation field. The meshfree method has inherent advantage for simulation of crack growth or representing a ‘fracturing’ interpolation field, because the interpolation field does not depend on mesh. In fact, a focal point of the early meshfree method (e.g. Belytschko et al. (1995)) is to develop the visibility condition algorithm that can serve as a criterion to automatically adapt the connectivity map of meshfree particles, so that the associated evolving interpolation field can represent growing crack surfaces. Li and Simonsen (2005) proposed a practical 2D parametric visibility condition algorithm in two-dimensional space. Following the same basic idea, Ren and Li (2010) proposed an algorithm to represent whole lifespan of crack growth including crack nucleation, propagation and arrest.

In this work, we are interested in crack growth in large scale thin plate and shell structures where the ratio between the plate span and plate thickness is  $>50$ .

To make the modeling and simulation simple, we make the following assumptions and approximations: (1) First, in this work we only deal with the through-thickness crack, so the crack tip always cuts through the thickness of the plate. In the meshfree discretization, we place several layers of particle along the thickness direction of the plate or shell, and we call a particle array that is perpendicular with the plate surface as a fiber, e.g. the red<sup>1</sup> line shown in Fig. 1(a) and (b). Hence each particle at the plate surface corresponds a fiber that is perpendicular to the plate surface, and each fiber has  $n$  particles along its axial direction. In general the plate may be discretized by  $n$  layers of meshfree particles, and in all the simulations done in this work we choose  $n = 3$ .

(2) The 3D crack surface may be represented by piece-wise plane facets constructed by the particles on crack surface as shown in Fig. 2(b). Here the particles on crack surface are marked as red diamonds, except the one at the crack tip, which is marked as blue square, whereas the normal meshfree particles are represented as black circles.

(3) In our approach, the crack tip is always attached to a fiber, which means it only moves from fiber to fiber.

<sup>1</sup> For interpretation of colour in Figs. 1, 2 and 6, the reader is referred to the web version of this article.

The macro-scale ductile crack growth criterion is postulated as a material damage criterion. In specific, we measure the material damage state of all the particles surrounding the current crack tip, and subsequently we can calculate the accumulated damage value for any fiber near the current crack tip. If the damage value at one particular fiber exceeds the critical value, we then declare it as the new crack tip, and subsequently, a crack length increment is performed, and the crack tip moves from old position to a new position.

In this work, we first choose either the volume fraction of voids, or the effective plastic strain as the damage measure  $D$ . We then choose a radial distance  $R$ , and draw a circle centered at the current crack tip on the plate surface shown as the blue circle in Fig. 1(a). Subsequently we can compute the damage value for each particles inside the thin circular slice volume encircled by the blue line. Now we can determine the damage value for each fiber inside the circular slice by adding the damage value of each particle along the fiber. For example, the variable  $D_j$  of fiber  $J$  is defined as sum of damage values of each particle on the fiber  $J$ , i.e.  $D_j = \sum_{i=1}^M D_{ji}$ , here  $M = 3$  as shown in Fig. 1. We then apply the crack growth criterion:  $D_j \geq D_c, \forall j = 1, \dots, n_p$  for every fiber inside the circle slice. If there is a fiber  $J$  such that the condition  $D_j > D_c$  holds, we then choose the fiber  $J$  as the new crack tip.

In practice, however, if the new crack tip is located behind the current crack tip, it could lead to some complications such as crack-direction-reverse phenomenon. To simplify the crack approximation algorithm, we limit the potential new crack tip inside a fan region  $\theta_c$  in the blue circle, shown as in Fig. 1(a). Here the vector  $\mathbf{V1}$ , which points from the previous crack tip to the current crack tip, is shown as a dashed vector, and the angle  $\theta$  is defined between the vector  $\mathbf{V2}$  (from the current crack tip to particle inside circle) and vector  $\mathbf{V1}$ . Finally, the new crack tip will be selected by criterion,

$$D_j \geq D_c \quad \text{and} \quad -\theta_c/2 \leq \theta \leq \theta_c/2 \quad (20)$$

When using the criterion, Eq. (20), the computational accuracy of predicting crack growth mainly depends on an appropriate damage criterion. Moreover, an obvious limitation of this criterion is that the crack reverse phenomenon is not considered.

### 3.2. Crack surface representation in plates

Once the new crack tip (a fiber) is selected, the old crack tip (a fiber) will be split to two fibers, i.e., all particles in that fiber should be split into two particles in order to form two new fibers. The particle splitting algorithm must keep conservation of volume, mass, and kinematic energy. Assume that the previous crack orientation vector ( $\mathbf{V1}$  in Fig. 1) and current crack orientation ( $\mathbf{V2}$  in Fig. 1) split the computational domain into two part with angles  $\phi_1$  and  $\phi_2$ , as shown in Fig. 1. The mass and volume of the new particles are re-assigned according to the following rules,

$$Mass_{new1} = \frac{\phi_1}{2\pi} Mass_{old} \quad (21)$$

$$Mass_{new2} = \frac{\phi_2}{2\pi} Mass_{old} \quad (22)$$

$$Volume_{new1} = \frac{\phi_1}{2\pi} Volume_{old} \quad (23)$$

$$Volume_{new2} = \frac{\phi_2}{2\pi} Volume_{old} \quad (24)$$

The kinematic field variables, such as original position, displacement, velocity, and acceleration of the new particles are assigned according to,

$$\mathbf{X}_{new1} = \mathbf{X}_{old} + \delta \quad (25)$$

$$\mathbf{X}_{new2} = \mathbf{X}_{old} - \delta \quad (26)$$

$$\mathbf{Disp}_{new1} = \mathbf{Disp}_{old} + \delta \quad (27)$$

$$\mathbf{Disp}_{new2} = \mathbf{Disp}_{old} - \delta \quad (28)$$

$$\mathbf{Vel}_{new1} = \mathbf{Vel}_{old} \quad (29)$$

$$\mathbf{Vel}_{new2} = \mathbf{Vel}_{old} \quad (30)$$

$$\mathbf{Acc}_{new1} = 0.0 \quad (31)$$

$$\mathbf{Acc}_{new2} = 0.0 \quad (32)$$

where  $\delta$  is a vector that is perpendicular to the new crack orientation  $\mathbf{V2}$  at plate surface and  $|\delta| \ll 1$ . By using this particle splitting procedure, the old particle  $\mathbf{X}_{old}$  on the outer surface of a shell is split to two new particles ( $\mathbf{X}_{new1}$  and  $\mathbf{X}_{new2}$ ) with a tiny spatial distance between them in reference configuration, in which the 3D parametric visibility algorithm is used. After particle splitting, the old crack tip fiber will be split into two new fibers, and there is a small distance between them, shown as Fig. 2(a), where the old crack tips are marked as black squares.

### 3.3. 3D parametric visibility condition algorithm

The objective of the particle splitting algorithm is to separate crack tip into two sets of particles in order to form new crack surfaces in physical space. In numerical simulations, the most crucial step is how to adjust interpolation field surrounding the growing crack tip to represent material separation in a computational domain. In contrast with FEM interpolation, meshfree interpolation relies on a local connectivity map to associate one particle with its neighboring particles. Therefore there must be an artificial algorithm to ‘cut off’ the interpolation connection of particles due to crack surface. In the 2D problem, Li and Simonsen (2005) consider the crack surface as piece-wise straight line segments. They proposed a 2D parametric visibility condition algorithm to re-interpolate the computational domain. Following a similar philosophy, in this work we propose a 3D parametric visibility condition algorithm, which can adjust meshfree interpolation field along crack surfaces in three-dimensional space.

For macro-scale fracture problems, the crack surface can be treated as an opaque wall, which may be figuratively thought as a medium that blocks the sight between two particles in two sides of the crack surface. In Fig. 2(a) the dashed vectors denote the sights that are blocked by crack surface. From Fig. 2, one can find the old crack tip fiber (marked as black square) located at the middle of crack surface at reference configuration. This paper approximates the crack surface as piece-wise plane facets, one can construct triangle plane facets by old crack tip fibers which are always located in the middle of crack surfaces as shown in Fig. 2(b), here the dashed triangle facets is constructed by connecting the first and last particles of crack tip fibers. In meshfree interpolation, every particle has its own local connectivity map to define its neighboring particles, once the line segment between a specified particle and its neighboring particle intersects with the crack surface (the dashed vector in Fig. 2(a)), we say that these two particles cannot ‘see’ each other. Then this neighboring particle must be removed from the local connectivity map of the particle. Since crack growth is incremental, one only needs to check and modify the connectivity maps for a limited number of particles or quadrature points around the current crack tip.

The crack growth algorithm in 3D shell structures presented here is designed for through-thickness cracks, which can be accomplished by the modification of the local connectivity map of specified particles that are identified by using geometric interception test between the line segment (Fig. 2(a)) and the triangle surface element (Fig. 2(b)). In practice, since the triangle element is composed of triangle facets, we can test the facets one by one, eventually the meshfree re-interpolation update can be proceed as we sort out visibility relations among all neighboring particles

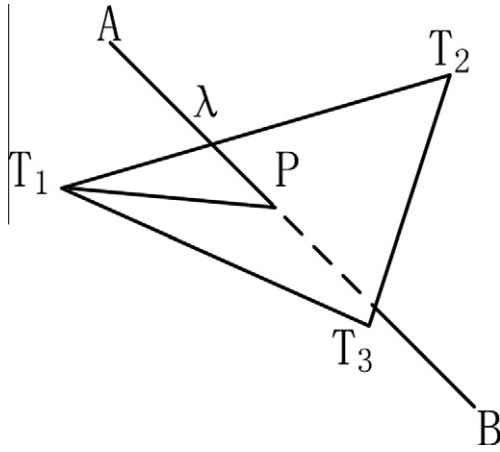


Fig. 3. 3D parametric visibility condition.

through the interrelation between line segments and triangle facets. The 3D parametric visibility algorithm is based on the geometric relation between a line segment with the end points  $\mathbf{A}(X_A, Y_A, Z_A)$ , and  $\mathbf{B}(X_B, Y_B, Z_B)$ , and a triangle facet with vertices  $\mathbf{T}_i(X_i, Y_i, Z_i)$ ,  $i = 1, 2, 3$ , which is explicitly illustrated in Fig. 3.

To begin with the test, we can first define two vectors  $\mathbf{T}_1\mathbf{T}_2(X_2 - X_1, Y_2 - Y_1, Z_2 - Z_1)$  and  $\mathbf{T}_1\mathbf{T}_3(X_3 - X_1, Y_3 - Y_1, Z_3 - Z_1)$  on a triangle facet. Then the normal vector of the triangle facet is,

$$\mathbf{N} = \mathbf{T}_1\mathbf{T}_2 \times \mathbf{T}_1\mathbf{T}_3 \tag{33}$$

In 3D space, the general relationships between a line segment and a triangle has three scenarios:

1. A line segment is in parallel with a triangle facet, but not in the triangle facet plane. The condition may be stated as,

$$\mathbf{N} \cdot \mathbf{AB} = 0 \quad \text{and} \quad \mathbf{T}_1\mathbf{A} \cdot \mathbf{N} \neq 0 \tag{34}$$

If the condition, Eq. (34), holds, it means that **particle A can ‘see’ particle B**;

2. If, however,

$$\mathbf{N} \cdot \mathbf{AB} = 0 \quad \text{and} \quad \mathbf{T}_1\mathbf{A} \cdot \mathbf{N} = 0 \tag{35}$$

this means that the line segment AB is actual in the triangle facet plane. Even though this is a special case, this case is not simple. One the other hand, however, in this case, the 3D visibility condition will degenerate to the 2D parametric visibility condition, because we can basically use the 2D visibility condition presented in Li and Simonsen (2005) and Simkins and Li (2006) to test whether or not the line segment AB intersects any one of the three sides of the triangle. To do this in a general 3D plane is tedious. In actual computations, an orthogonal projection decomposition method is used, in which the triangle facet plane is project to three Cartesian coordinate planes,  $X_1OX_2, X_1OX_3, X_2OX_3$ . In general, the triangle facet in space will have three affine projection images on those three coordinate planes, unless they are in perpendicular. For instance, if  $\mathbf{N} \cdot \mathbf{E}_k \neq 0$ , a particle  $\mathbf{A}(x_1, x_2, x_3)$  in 3D space can be projected to 2D space  $\mathbf{E}_i \otimes \mathbf{E}_j (i, j \neq k)$  with coordination  $(x_i, x_j)$ , and this particle can be the intersection point  $\mathbf{P}$  or one of the three vertices of the triangle. After the orthogonal projection decomposition, we use the 2D visibility condition presented in Li and Simonsen (2005) to test the visibility condition between the projection image of the line AB and the images of three sides of the triangle.

If all tests are passed, we can say that particle **A can ‘see’ particle B**.

3. The last scenario is the case that the line segment AB actually intersects the triangle facet plane. In this case, we first find the

intersection point between the line segment and the triangle facet plane, and we label the intersection point as  $\mathbf{P}$ .

We can then try to determine whether the point  $\mathbf{P}$  is inside the triangle or not. The detailed testing procedure is outlined as follows: If  $\mathbf{N} \cdot \mathbf{AB} \neq 0$ , the line segment AB is not parallel with the triangle facet, we can define a vector  $\Delta$  as,

$$\Delta = \mathbf{B} - \mathbf{A} \tag{36}$$

Assume that the line segment  $\mathbf{AB}$  intersects with the **plane of triangle facet** at the point  $\mathbf{P}$  (one triangle facet can define one plane) at  $\mathbf{P} = \mathbf{A} + \lambda\Delta$  with parameter  $\lambda$  as shown in Fig. 3. Since  $\mathbf{P}$  is located on the plane of the triangle facet, we have,

$$\mathbf{N} \cdot \mathbf{T}_1\mathbf{P} = 0 \tag{37}$$

where  $\mathbf{T}_1\mathbf{P}$  is defined as the line segment,  $\mathbf{A} - \mathbf{T}_1 + \lambda\Delta$  as shown in Fig. 3. From Eq. (37), the parametric  $\lambda$  can be solved as,

$$\lambda = \frac{(X_1 - X_A)[\overline{YZ}_1^{23} - \overline{YZ}_1^{32}] + (Y_1 - Y_A)[\overline{ZX}_1^{23} - \overline{ZX}_1^{32}] + (Z_1 - Z_A)[\overline{XY}_1^{23} - \overline{XY}_1^{32}]}{\Delta_x[\overline{YZ}_1^{23} - \overline{YZ}_1^{32}] + \Delta_y[\overline{ZX}_1^{23} - \overline{ZX}_1^{32}] + \Delta_z[\overline{XY}_1^{23} - \overline{XY}_1^{32}]} \tag{38}$$

where  $\overline{YZ}_k^{ij} = (Y_i - Y_k)(Z_j - Z_k)$ ,  $\overline{ZX}_k^{ij} = (Z_i - Z_k)(X_j - X_k)$ ,  $\overline{XY}_k^{ij} = (X_i - X_k)(Y_j - Y_k)$ ,  $i, j, k = 1, 2, 3$ . If  $\lambda < 0$  or  $\lambda > 1$ , the line segment AB does not intersect with the triangle facet plane, even though they are not in parallel. In this two cases, **the particle A can see particle B**.

If  $0 \leq \lambda \leq 1$ , it is then that the line segment does intersects the triangle facet plane at the point  $\mathbf{P}$ . Now the point  $\mathbf{P}$  may locate either inside or outside of the triangle facet, or on the surface of the triangle facet as shown in Fig. 4. Hence we have to conduct further tests to judge the visibility. The point  $\mathbf{P}$  and any two vertices of the triangle facet can form three new triangle facets in total. We can define the normal of these new triangle facets as:

$$\mathbf{N}_1 = \mathbf{PT}_1 \times \mathbf{PT}_2 \tag{39}$$

$$\mathbf{N}_2 = \mathbf{PT}_2 \times \mathbf{PT}_3 \tag{40}$$

$$\mathbf{N}_3 = \mathbf{PT}_3 \times \mathbf{PT}_1 \tag{41}$$

We have the following visibility condition: if

$$\mathbf{N} \cdot \mathbf{N}_1 \geq 0 \quad \text{and} \quad \mathbf{N} \cdot \mathbf{N}_2 \geq 0 \quad \text{and} \quad \mathbf{N} \cdot \mathbf{N}_3 \geq 0 \tag{42}$$

the point  $\mathbf{P}$  locates inside the triangle facet, and hence **particle A cannot ‘see’ particle B**. Otherwise, **particle A can ‘see’ particle B**. Some of these conditions are illustrated in Fig. 4.

In computations, the condition that **particle A can ‘see’ particle B** means that the particle  $\mathbf{B}$  will remain in the local connectivity group of the particle  $\mathbf{A}$ . In contrast with the fact that **particle A cannot ‘see’ particle B**, which means that the particle  $\mathbf{B}$  will be removed from the local connectivity group of the particle  $\mathbf{A}$ .

In the following example, we illustrate how a shape function of a particle changes when it is located along a crack path. When the crack just reached the particle, the original shape function of the particle is shown in Fig. 5(a). The meshfree interpolation field is a 3D distribution field, and to illustrate this 3D field clearly, we use the color contour intensity indicates the height or value of the shape function. For visualization purpose, we set the 3D computational domain transparent. At the beginning the crack surface does not ‘cut off’ any local connectivity of neighboring particles at the crack tip. Consequently, the shape function has finite values both inside the solid as well as on the crack surface (the dark shadow). After the crack passes through that particle, the particle is split into two new particles on newly formed crack surface, and this is done by the particle splitting algorithm to enact surface separation.

In numerical simulation, this leads to modification of local connectivity map by using the 3D parametric visibility condition. In Fig. 5(b) and (c), one can find that the shape functions of the newly split particles of the old crack tip only have values in their part of

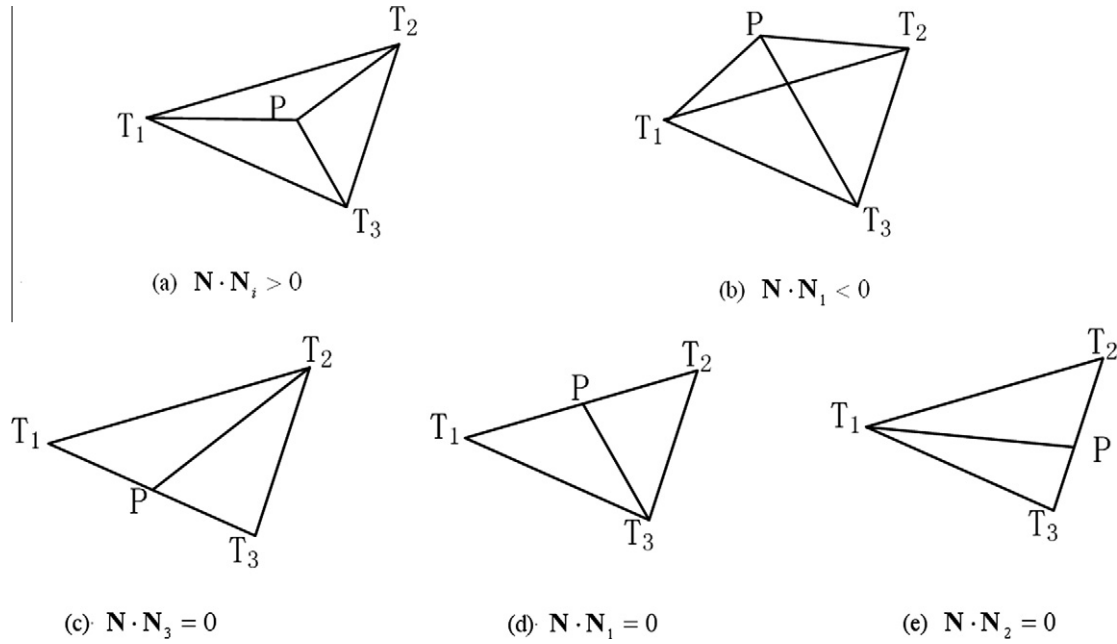


Fig. 4. Spatial relation between P and triangle facet.

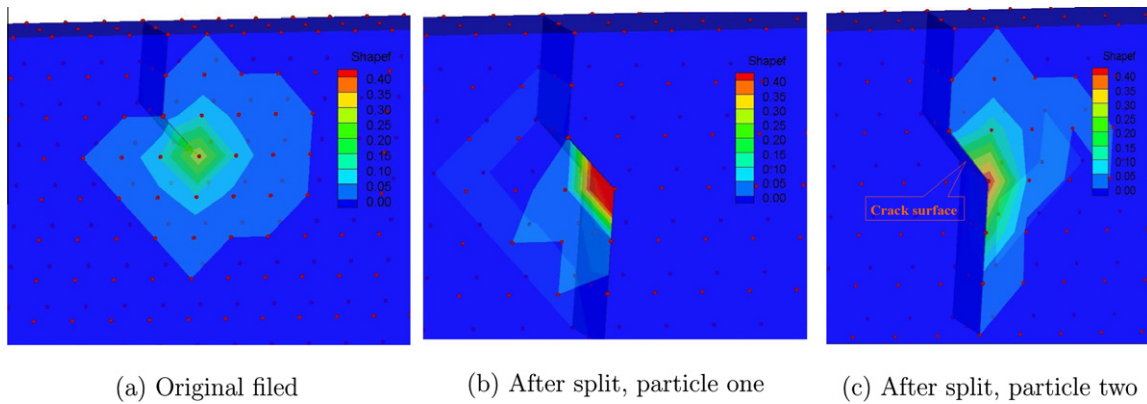


Fig. 5. Meshfree shape function evolution along crack propagation.

the half body, and they do not spread across crack surface. This illustrates that the proposed 3D parametric visibility condition algorithm can automatically update the local connectivity map and consequently interpolation field while a crack grows.

#### 4. Gurson-type of ductile damage models

Both the Gurson type plasticity damage models and the Johnson–Cook plasticity damage model have been extensively used in modeling ductile materials and their failure analysis. In this section, we first discuss various Gurson type models, and their constitutive update in simulations.

##### 4.1. The Gurson-type constitutive models

###### (1) Original Gurson model

The basic assumption of the Gurson model is that deviatoric stress state controls plastic yielding while triaxial stress state controls the damage progress with the mechanism of void growth of coalescence (Rice and Tracey, 1969; Nielsen and Tvergaard, 2010).

The yield surface of the Gurson Model (Gurson, 1977; Nahshon and Hutchinson, 2008) is given as follows,

$$\Phi(\sigma_e, \sigma_m, f) = \left(\frac{\sigma_e}{\sigma_M}\right)^2 + 2q_1 f \cosh\left(\frac{3q_2}{2} \frac{\sigma_m}{\sigma_M}\right) - (1 + q_3 f^2) \quad (43)$$

where  $\sigma_e = \sqrt{\frac{3}{2} \mathbf{s} : \mathbf{s}}$  is the effective stress of the deviatoric stress tensor  $\mathbf{s} = \boldsymbol{\sigma} - \sigma_m \mathbf{I}$ ,  $\sigma_m = \sigma_{kk}/3$ . While,  $\sigma_M$  is the microscopic yield stress in the matrix material surrounding voids, i.e. the material between voids. Throughout this paper, all quantities with subscript  $M$  represent the state of matrix material at micro-scale. In Eq. (43)  $q_1, q_2, q_3$  are material constants.

For incompressible matrix materials, the rate of void growth can be found as,

$$\dot{f} = \dot{f}_g = (1 - f) d_{kk}^p \quad (44)$$

where  $d_{kk}^p$  is the trace of plastic rate of deformation.

###### (2) Gurson–Tvergaard–Needleman (GTN) model

The Gurson–Tvergaard–Needleman (GTN) model (Tvergaard and Needleman, 1984) is a simulation-based plasticity–damage model, which takes into account of the effect of rapid void coalescence at failure phase. In particular, Tvergaard and Needleman

(1984) proposed a function  $f^*(f)$  that replaces the variable  $f$  in Eq. (43),

$$f^*(f) = \begin{cases} f & f \leq f_c \\ f_c + \frac{1/q_1 - f_c}{f_f - f_c} (f - f_c) & f_c < f \leq f_f \\ 1/q_1 & f > f_f \end{cases} \quad (45)$$

The void growth rate consists of growth of existing voids and nucleation of new voids, i.e.

$$\dot{f} = \dot{f}_g + \dot{f}_n \quad (46)$$

where  $\dot{f}_g$  is defined in Eq. (44). Considering the plastic strain rate induced nucleation, we have

$$\dot{f}_n = A_N \dot{\epsilon}_M^p \quad (47)$$

Here the nucleation strain follows a normal distribution with a mean value  $\epsilon_N$  and a standard deviation  $s_N$  (Chu and Needleman, 1980):

$$A_N = \frac{f_N}{s_N \sqrt{2\pi}} \exp \left[ -\frac{1}{2} \left( \frac{\epsilon_M^p - \epsilon_N}{s_N} \right)^2 \right] \quad (48)$$

where  $f_N$  is the volume fraction to nucleate voids.

### (3) Shear modified Gurson (SM-Gurson) model

In above two models, the rate of void growth is solely determined by dilatational plastic strain rate as shown in Eq. (44), which is the basic assumption of the Gurson model. A major limitation of the Gurson model, which has become apparent in recent years, is its inability to capture strain localization and ductile fracture for shear stress-dominated problems such as plugging failure during projectile penetration, cropping, or dynamic shear-off. According to the Gurson model or the GTN model, an increase in  $f$ , i.e. the incremental growth in volume fraction of voids, requires a positive mean stress. Whereas in the cases of shear-dominated deformations with zero or negative mean stress, the model predicts no increase in damage if there is no continuous void nucleation. As a consequence, the model predicts that no damage induced softening will take place under shear in materials with inherent strain hardening capacity, and hence neither localization nor material failure can occur in this case, which is obviously not realistic (Nahshon and Hutchinson, 2008).

Considering the fact that the damage mechanisms such as void distortion and inter-void interaction under deviatoric stress state may also give rise to strain softening and localization, Nahshon and Hutchinson (2008) modified the damage mechanism of the Gurson model by adding the damage effect due to the deviatoric stress,

$$\dot{f}_s = k_w f \omega(\sigma) \frac{\mathbf{s} : \mathbf{d}^p}{\sigma_e} \quad (49)$$

where

$$\omega(\sigma) = 1 - \left( \frac{27J_3}{2\sigma_e^3} \right)^2 \quad (50)$$

with  $J_3 = |\mathbf{s}|$ . Subsequently, the growth rate of void volume fraction becomes,

$$\dot{f} = \dot{f}_g + \dot{f}_n + \dot{f}_s \quad (51)$$

here  $\dot{f}_g$  and  $\dot{f}_n$  are defined in Eqs. (44) and (47) respectively. The SM-Gurson model uses the same plastic flow function as the GTN model.

### (4) The Modified Gurson Model (M-Gurson)

It is generally believed that for moderate and high stress triaxiality ( $T = \sigma_m / \sigma_e$ ) state, the GTN model can accurately describe ductile fracture process of metallic materials; and when stress

triaxiality is low, the SM-Gurson model should be used because the damage contribution due to shear stress become significant as discussed above. As Nielsen and Tvergaard (2009) argued, the additional damage contribution from shear stress, i.e.  $\dot{f}_s$ , may have too strong effect when stress triaxiality is high. To model both the ductile plug failure and interfacial shear failure simultaneously, Nielsen and Tvergaard (2010) recently modified the equation of  $\dot{f}_s$  to make the extra shear contribution dependent on the level of stress triaxiality, while keeping the other features of the SM-Gurson model,

$$\dot{f}_s = k_w f \omega_0 \frac{\mathbf{s} : \mathbf{d}^p}{\sigma_e} \quad (52)$$

and,

$$\omega_0 = \omega(\sigma) \Omega(T) \quad (53)$$

where  $\omega(\sigma)$  is defined in Eq. (50),  $\Omega(T)$  is a function of stress triaxiality,

$$\Omega(T) = \begin{cases} 1 & T < T_1 \\ \frac{T - T_2}{T_1 - T_2} & T_1 \leq T \leq T_2 \\ 0 & T > T_2 \end{cases} \quad (54)$$

Eq. (54) sets up an option rule that the SM-Gurson model is used when  $T < T_1$ , and the GTN model will be used when  $T > T_2$ .

## 4.2. Constitutive update

The plastic flow function in Eq. (43) contains the yield stress of matrix at micro-scale ( $\sigma_M$ ), macro-scale effective stress  $\sigma_e$ , and macro-scale mean stress  $\sigma_m$ . The rate of void volume growth is related to the rate of deformation and micro-scale yield stress as well. These features make the constitutive update very complex in 3D explicit time integration. In this paper, the elastic trial and relaxation approach of Aravas (1987) is adopted. For interested readers, they may consult Simonsen and Li (2004), which has provided a detailed constitutive update equations for GTN model for 2D problems. In the present work, we basically follows Simonsen and Li (2004) to establish the formulations for constitutive update of different Gurson models with the different hardening laws for 3D simulations.

Typically, ductile steels are modeled by power-law hardening. To simplify the derivation, in this work, an isotropic hardening modulus  $h_M$  is chosen as the function of logarithmic plastic strain  $\epsilon_M^p$  and the true stress  $\sigma_M$ , and it can result a fairly accurate simulations. However, to obtain more accurate simulation results, the power-law hardening may have to be implemented with exact material hardening constants.

$$h_M = \frac{d\epsilon_M^p}{d\sigma_M} \quad (55)$$

The detailed constitutive update is outlined in Appendix A and B.

## 5. Johnson–Cook model and its constitutive update

The Johnson–Cook model (Johnson and Cook, 1983, 1985), is a rate-dependent thermo-mechanical constitutive model, which has been extensively used in simulations of ductile fracture induced by high strain rate loading such as shock waves and high speed impacts. The thermo-mechanical coupled meshfree Galerkin formulation are not described in this paper, and interested readers can refer to Ren and Li (2010) for details.

In the Johnson–Cook model, the effective plastic strain rate is defined as:

$$\dot{\bar{\epsilon}} = \dot{\epsilon}_0 \exp \left\{ \frac{1}{C} \left( \frac{\sigma_M}{g(\bar{\epsilon}, T)} - 1 \right) \right\} \quad (56)$$

$$g(\bar{\epsilon}, T) = (A + B\bar{\epsilon}^n)(1 - \Gamma^m), \quad \text{with} \quad \Gamma = \frac{T - T_0}{T_m - T_0}$$

where  $\dot{\epsilon}_0$  is referential strain rate, and normally it is chosen as  $1.0 \text{ s}^{-1}$ ,  $n$  and  $m$  are strain hardening and thermal softening parameters.  $T_0$  and  $T_m$  are room and melting temperature respectively.

For thermo-mechanical coupled problem, the total deformation can be decomposed to elastic, plastic, and thermal parts, as shown in Eq. (4). In case of isotropic hardening, the plastic strain rate is,

$$\mathbf{d}^p = \dot{\bar{\epsilon}} \hat{\mathbf{n}} \quad (57)$$

In adiabatic heating, the rate of deformation induced by thermal effect is,

$$\mathbf{d}^t = \frac{\gamma\chi}{\rho C_p} \sigma_e \dot{\bar{\epsilon}} \mathbb{I} \quad (58)$$

where  $\gamma$  is the coefficient of thermal expansion,  $\chi$  denotes the fraction of plastic work converting to heat,  $C_p$  is specific heat, and  $\mathbb{I}$  denotes the second order unit tensor.

The rate form of constitutive equation with thermal effect can be expressed as,

$$\nabla \cdot \boldsymbol{\sigma} = \mathbf{C} : \mathbf{d}^e = \mathbf{C} : (\mathbf{d} - \mathbf{d}^p - \mathbf{d}^t) \quad (59)$$

For explicit time integration, the stress and strain fields at time  $t_{n+1}$  are updated from the state at time  $t_n$ . Choosing the Jaumann rate as the objective rate in Eq. (59), the time stress derivative of the Cauchy stress can be found as,

$$\dot{\boldsymbol{\sigma}}_{n+1} = \nabla_n \cdot \mathbf{w}_n \cdot \boldsymbol{\sigma}_n - \boldsymbol{\sigma}_n \cdot \mathbf{w}_n^T \quad (60)$$

Then the stress state can be updated by,

$$\boldsymbol{\sigma}_{n+1} = \boldsymbol{\sigma}_n + \dot{\boldsymbol{\sigma}}_{n+1} \Delta t \quad (61)$$

The crack propagation algorithm in Section 3 needs a damage indicator in order to determine crack growth process. The Gurson model has the damage parameter  $f$  that can be used in the crack growth algorithm. For the Johnson–Cook model, an accumulative damage model (Simkins and Li, 2006) is adopted to estimate damage status of a material point, and hence a meshfree particle,

$$D = \sum \frac{\Delta \epsilon}{\epsilon_f}$$

$$\epsilon_f = \left[ D_1 + D_2 \exp \left( D_3 \frac{\sigma_m}{\sigma_M} \right) \right] \left[ 1 + D_4 \ln \dot{\bar{\epsilon}} \right] \left[ 1 + D_5 \Gamma \right] \quad (62)$$

where  $\Delta \epsilon$  is the plastic strain increment in one time step, and  $D_1, D_2, D_3, D_4, D_5$  are material constants.

## 6. Numerical simulations

### 6.1. Calibration with large scale in-plate tearing experiment

Although there has been much effort using finite element methods and meshfree methods in combination with the Gurson type of models to simulate ductile fracture in materials and structures, e.g. Mathur et al. (1996) and Li and Simonsen (2005), it is still a challenge to use numerical methods to capture and predict ductile fracture or progressive ductile failure in large scale engineering structures made by real engineering materials. The complexity and difficulty of simulating ductile structural failures are multi-tude, and it is affected by actual structural geometry, stiffness, and dimension. For instance, the crack nucleation and initial propagation in plate and shell structures is a size-dependent process, and a crack needs to grow to a length of few times greater than

the plate thickness before it can reach to stationary propagation condition.

To have a meaningful simulation, we closely validate our meshfree approach with the existing experimental data. In experiments, the standard fracture mechanics test specimens are relatively small, because it is intended to measure the material fracture toughness or material fatigue strength rather than the actual fracture event on an actual structure. In material fracture toughness test, the typical crack length in a specimen is about from a few millimeters to centimeters, which may not be appropriate for the testing of large scale crack propagation in engineering structures, because the fracture strength of a structure is not only dependent on material fracture toughness, but also dependent on overall structure stiffness. Simonsen and Tornqvist (2004) have conducted a fracture strength experiment of real size engineering structures under in-plane bending and stretching. The test can faithfully provide measurements for large-scale ductile fracture strength of a plate structure. The testing data measured in this experiment contain essential information of the crack growth, which can be related to structure strength; moreover they can also be calibrated and compared with the material constitutive model and numerical simulation. The detailed experimental set-up is shown as Fig. 6(a).

The main testing variables that are measured in the experiment are,

**P**: the crosshead load from the testing machine

$\Delta$ : the crosshead displacement from the testing machine

In the meshfree simulation, the clamp system is considered as rigid, the specimen is discretized by 5073 particles and 25600 quadrature points, and a pre-set crack is prescribed in the initial configuration. The integration time step is,  $\Delta t = 10^{-7} \text{ s}$ , the computing domain is shown in Fig. 6(b), and there are three layers of particles distributed along thickness direction of the plate, i.e., one fiber is composed of three particles. In the experiment, a displacement-controlled loading is imposed and measured as the crosshead displacement  $\Delta$ . To compare with the simulation results, this displacement-controlled boundary condition must be translated to a prescribed displacement boundary condition for meshfree computation (see Fig. 6(b)). Since the clamp is considered as rigid, and it will rotate about an axis (the point **O** in Fig. 6(a)). A 2D Cartesian coordinate system can be constructed with that axis as origin, and the rigid clamp is represented by a triangle ( $\Delta ABO$  with  $A(x_1, y_1)$ ,  $B(x_3, y_3)$ ) shown as the red triangle in Figs. 6(a) and 7. From Fig. 6(a), we can find the line segment AB is the side of plate where essential boundary is imposed. The boundary displacement  $\Delta$ , which moves along Y axis, is imposed at point A, and  $\Delta ABO$  will rotate to ( $\Delta A'B'O$  with  $A'(x_2, y_2)$ ,  $B'(x_4, y_4)$ ). At original position, the length of OA and angle  $\alpha$  are defined as:

$$\alpha = \arctan \frac{y_1}{x_1} + \pi \quad (63)$$

$$l = \sqrt{x_1^2 + y_1^2} \quad (64)$$

The displacement boundary  $\Delta$  can be defined as,

$$\Delta = y_2 - y_1 = l \sin(\alpha - \beta) - l \sin(\alpha) \quad (65)$$

where  $\beta$  is the rotated angle:

$$\beta = \alpha - \left( \pi - \arcsin \left( \frac{\Delta}{l} + \sin(\alpha) \right) \right) \quad (66)$$

A point inside AB can be defined as,  $\mathbf{X}(x, y)$ , the length of  $\vec{OX}$  and angle  $v$  are,

$$l_1 = \sqrt{x^2 + y^2} \quad (67)$$

$$v = \arctan \frac{y}{x} + \pi \quad (68)$$

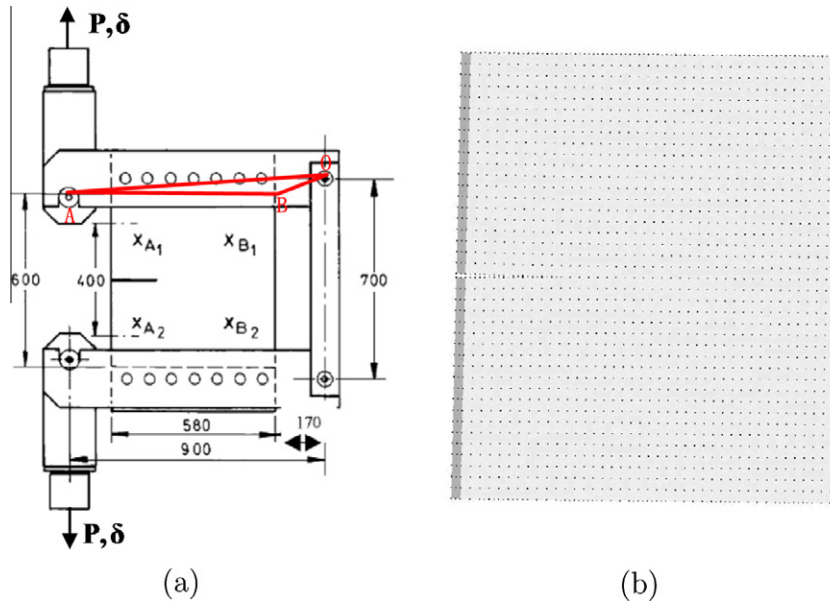


Fig. 6. (a) Experimental set-up for large scale fracture testing of plates (From Simonsen and Tornqvist (2004)) and (b) meshfree discretization domain.

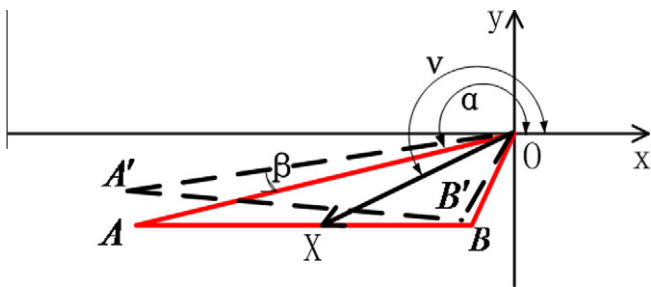


Fig. 7. Illustration of boundary condition.

Then the displacement boundary at point  $X$  can be calculated as,

$$\Delta x = l_1 \cos(v - \beta) - l_1 \cos v \quad (69)$$

$$\Delta y = l_1 \sin(v - \beta) - l_1 \sin v \quad (70)$$

From the experimental specimen configuration shown in Fig. 6(a), one can find that  $x_1 = -900$ ,  $y_1 = -50$ ,  $x$  ranges from  $-170$  to  $-750$ ,  $y = -50$  with unit mm. From existing literatures, we cannot find material constants in the Gurson model for Normal Strength

Table 1  
The material constants for Normal Strength steel.

Parameter	Value	Definition
$E$	200 GPa	Young's modulus
$\nu$	0.3	Poisson's ratio
$\rho$	7800 kg m <sup>-3</sup>	Mass density
$\sigma_M^0$	270 MPa	Initial yield stress
$h_M$	833 MPa	Hardening modulus
$q_1$	2.5	Gurson parameter1
$q_2$	1.0	Gurson parameter2
$q_3$	3.25	Gurson parameter3
$f_0$	0.0025	Initial void volume fraction
$f_N$	0.02	Void nucleation parameter
$\epsilon_N$	0.55	Void nucleation parameter
$s_N$	0.2	Void nucleation parameter
$f_c$	0.021	Void volume coalescence
$f_f$	0.2109	Void volume at failure
$k_w$	1.0	The coefficient of shear
$T_1$	0.2	Low Stress triaxiality
$T_2$	0.7	High Stress triaxiality

steel. We select material constants and the model parameters based on these following considerations: first the material constants  $E$ ,  $\rho$ ,  $\sigma_y$  for Normal Strength steel ( $f = 0$ ) are taken from the structural tensile test from Simonsen and Tornqvist (2004) that are tabulated in Table 1. Second, Nahshon and Xue (2009) reported the material constants of the SM-Gurson model for steel DH36, which are also calibrated with experimental data. Third, Nielsen and Tvergaard (2010) discussed the parameter  $T_1$  and  $T_2$  for DP600 steel. Based on these studies, we have conducted a series of simulations with different Gurson models to calibrate material constants for each of them based the experimental data obtained from Simonsen and Tornqvist (2004). The final set of material constants used for various Gurson models are listed in Table 1. By using the material constants listed in Table 1, the simulations of the plate tearing test have been carried out for (1) original Gurson model, (2) GTN model, (3) SM-Gurson model, (4) M-Gurson model (with a critical void volume fraction as the fracture criterion), and (5) a GTN model with a critical effective plastic strain as the fracture criterion.

In the first four models, the crack growth criterion is set as:  $D_c = f_p = 0.0135$ , and for the fifth simulation, the effective plastic shear criteria is set as  $D_c = \epsilon^p = 0.35$ . The experiment provides the dynamical crack history curve as crosshead loading  $\mathbf{P}$  against crosshead displacement  $\Delta$ . In these simulations, to get the equivalent loading at point  $A$  in Fig. 6(a), we use the moment balance between the loading force  $\mathbf{P}$  and the traction force at surface  $AB$  about point  $O$ . The numerical and experimental data are compared in Fig. 8. One may find that the total crosshead displacement is 0.12 m, which is a fracture test under large deformation for plate structure, in contrast with standard fracture mechanics test experiment, where the total displacement is at millimeter scale with a much smaller plate thickness for plan stress tests. From Fig. 8(a) and (b), at elastic phase, i.e, the stress state does not reach to the plastic yield surface, all different Gurson models give the same stress-strain relation. Therefore, all numerical curves overlap exactly at early stage as shown in Fig. 8(a). In Fig. 8(b) one may find the overlapped region between the GTN model (the dark curve) and SM-Gurson model (the dashed SM-Gurson curve). Once the deformation reaches the initial yield point, the increasing plastic deformation will result the increase in void growth rate, i.e. void volume fractions  $f$ , which are different with respect to various Gurson models. Consequently, the predicted stress-strain curve

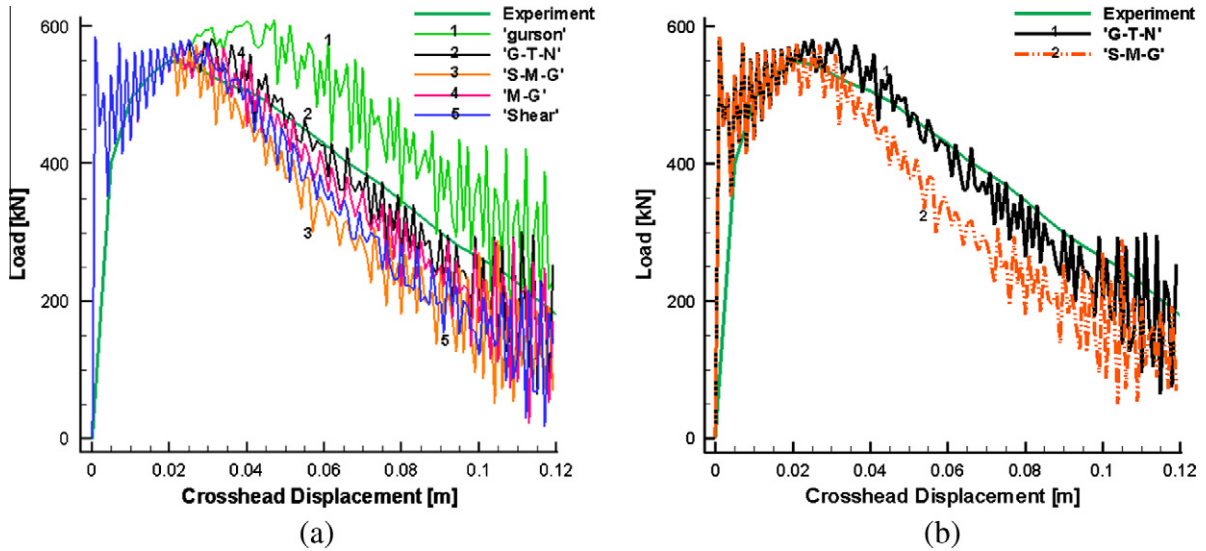


Fig. 8. Comparison of dynamic fracture history with experiment and simulation. (a) the comparison of experiment with various Gurson models; (b) the comparison of experiment with GTN and SM-Gurson.

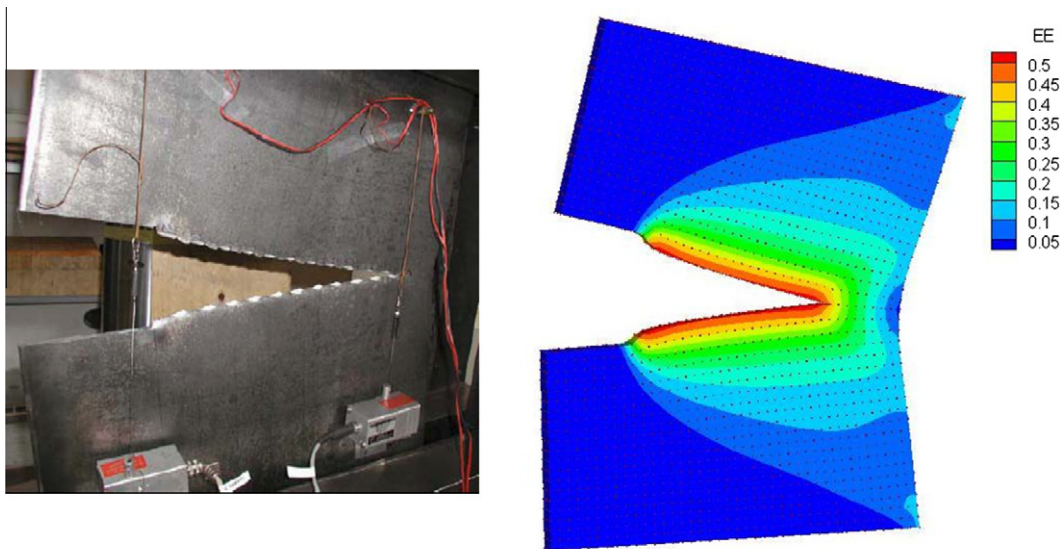
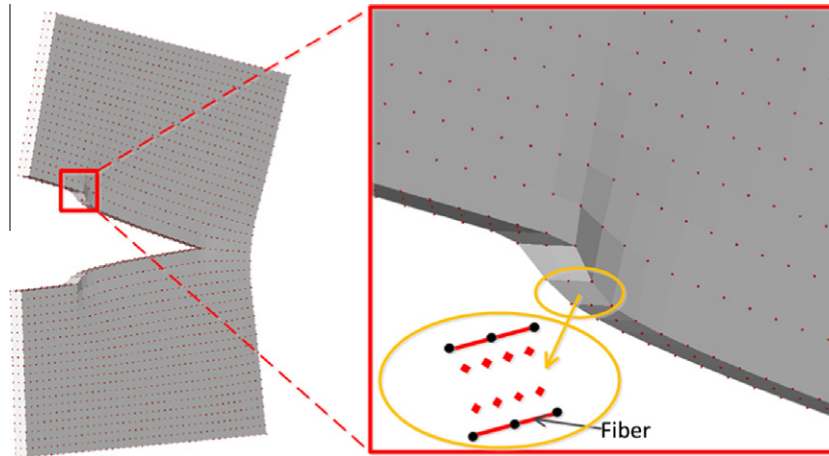


Fig. 9. Final fracture morphology of experimental (Simonsen and Tornqvist, 2004) and numerical simulation.

(relation) starts to differ. Original Gurson model do not consider the rate of void nucleation,  $f$  is smallest, therefore the material shows higher stiffness than experimental data. As mentioned in the pervious section, for SM-Gurson model, the shear stress contribution to damage may be too strong when material is at mediate and high stress triaxiality state. Since the experiment is basically a Model-I fracture test, therefore, in this case the SM-Gurson model predicts a much softer material response. Theoretically, for the Model I fracture problem, GTN model is the most appropriate material model, and therefore one may find that the numerical results of GTN model fits the experimental results best. The M-Gurson model makes an adjustment in the shear contribution when stress triaxiality is high, accordingly Fig. 8 shows that it compares with experimental data well. Based on Fig. 8, we believe that for mixture fracture model problem the M-Gurson model may perform better.

Moreover, one may find that in contrast with the smooth quasi-static experimental curve, there are distinct fluctuations in Fig. 8(a)

and (b), especially at the later stage of the test. The reason for such load-deflection curve fluctuation may be due to both dynamic effect as well as the numerical crack growth algorithm. The numerical simulations are conducted as a dynamic process with constant velocity (10 m/s) at crosshead as shown in Fig. 6(a). During the simulation, the effect of dynamic stress fields may lead to fluctuation on measured crosshead loading force. At the later stage of simulation, when the crack tip approaches to the boundary of specimen, the stress fields become complex with the reflection of stress wave, consequently it will result to higher fluctuations of the measured crosshead loading force. Moreover, in numerical simulation, the crack advances a fixed spatial spacing in one or several time steps, which is a discontinuous growth pattern, and this may attribute the fluctuation of load-deflection curve. Despite the dynamic effect or other numerical effects of the simulations, from Fig. 8(a) and (b), one can find that the overall trend of the numerical results fit well with the experimental data. In Fig. 9, we juxtapose the experimental crack morphology with that of



**Fig. 10.** Necking phenomenon at the pre-crack tip: black points are meshfree particles, and red points are quadrature points. (For interpretation of the references to colour in this figure legend, the reader is referred to the web version of this article.)

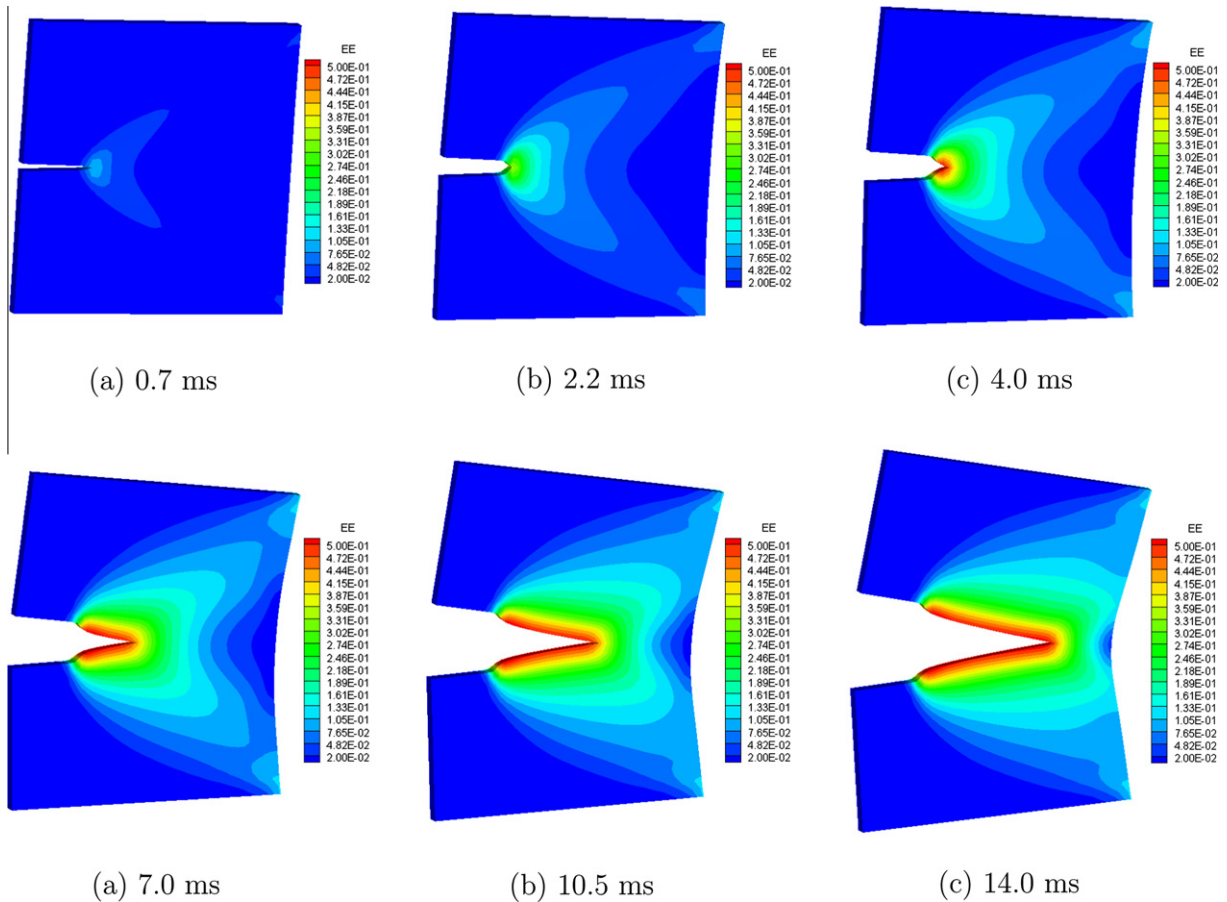


**Fig. 11.** Time sequence of the tearing test based on the M-Gurson model.

simulated crack. Again one may find that the simulation result compare well with the experimental result.

In the simulation of through-thickness crack growth, the stress distribution in transversal surface also affects the process of crack evolution. Therefore, there must be sufficient quadrature points along the thick direction of the plate in meshfree discretization. In this work each background element is integrated with  $2 \times 2 \times 2$  quadrature points. Considering a zone between two fibers (the yellow circle zone in Fig. 10), if one fiber consists of 3

particles, there are 4 layers quadrature points along the thickness direction. Zooming into the tip of pre-set crack, one may find the detailed deformation morphology nearby the crack tip, and it is clear that plastic tension instability or necking phenomenon occurs at the crack tip, see Fig. 10, which is similar to the experimental observation shown in Fig. 9. Although more particles in the thickness direction may raise the computation accuracy, computational efficiency will then be affected as well in terms of slow computational speed and increasing computational cost. For all

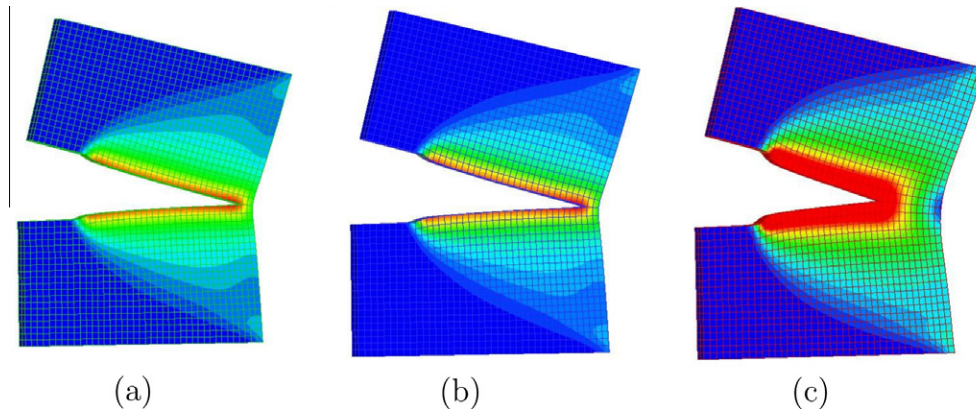


Fig. 12. Plastic strain distribution for different Gurson models: (a) GTN model, (b) M-Gurson model, and (c) SM-Gurson model.

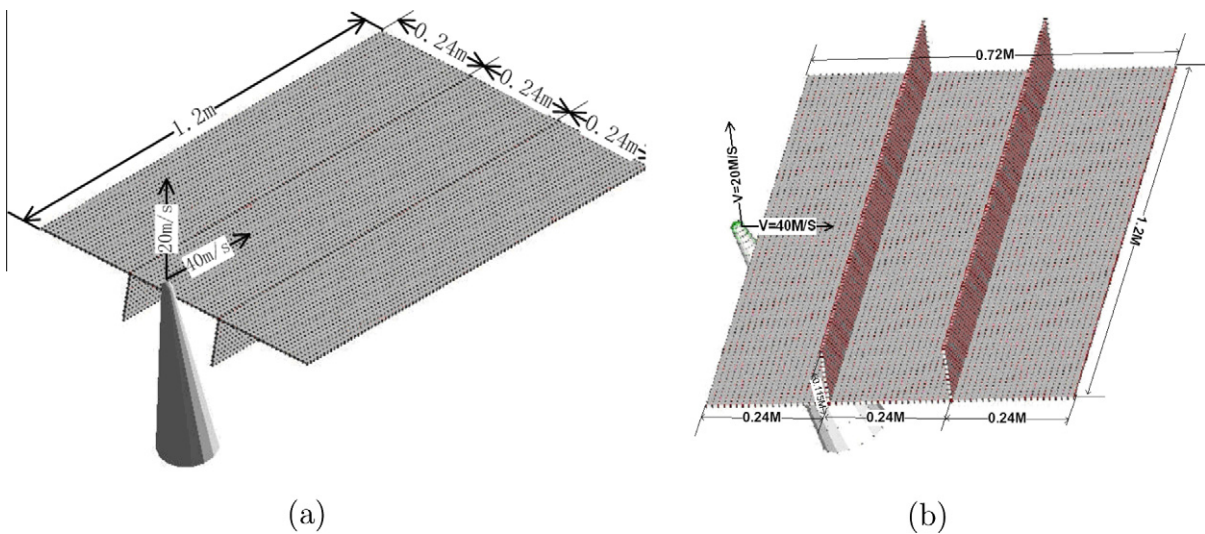


Fig. 13. The configuration of simulations: (a) Simulation I, and (b) Simulation II.

simulations reported in this paper, each fiber contains three particles.

The final fracture configurations of the specimen in both experimental and numerical simulations are juxtaposed in Fig. 9. One may find that they are compared well. In Fig. 9, the color contour on numerical specimen is the effective plastic strain, and one can find that high plastic strain distribution remains on the crack surface, which is the typical feature of ductile fracture.

In Fig. 11, we display a time sequence of a tearing test based on M-Gurson model. To compare the differences among the various Gurson's models, in Fig. 12, we juxtapose the numerical results (at  $t = 14$  ms) for three different Gurson's models, e.g. GTN model, the M-Gurson model, and the SM-Gurson model, and we compare them with the effective plastic strain distribution. One may find that (1) under the same loading condition, the SM-Gurson model predicts the most intense plastic strain around crack surfaces, and the GTN model predicts the least plastic strain. On the other hand, GTN model predicts the longest crack growth, the M-Gurson model predicts almost the same amount crack growth as GTN model does, whereas the SM-Gurson model predicts a much shorter crack growth than the previous two models.

It is important to note that not only we use this test to determine constitutive parameters, not also to determine the threshold damage value  $D_c$  for onset fracture in the plate structure, which

ensures that the postulated fracture criterion is supported by experiments.

## 6.2. Simulation I: crack propagation in a stiffened plate

The previous simulation calibrates material constants of the M-Gurson model for Normal Strength steel with in-plate tear experiment. However, realistic fracture phenomena in industry are induced by impact/contact, such as ship grounding (Simonsen, 1997). And the plate structure is normally stiffened to increase both stiffness and overall strength. The simulation of a plate with two flat bar stiffeners grounding with a rigid cone has been carried out in this work. This simulation is a simplified version of ship grounding problem discussed by Simonsen (1997), and it can investigate the abilities of the M-Gurson model and the proposed 3D parametric visibility condition algorithm in the realistic contact/damage engineering problem. The specimen is made of a 5 mm thickness plate, and there are two different configurations of the cone-shape rock/plate interaction as shown in Fig. 13(a) and (b). In Simulation I, we first consider the configuration of cone-shape rock/plate interaction shown in Fig. 13(a). Here the rigid cone impacts the plate structure with constant velocity (40 m/s, 20 m/s), the two edges of the plate that are perpendicular to the impacted edge are prescribed as fixed displacement boundary. There are

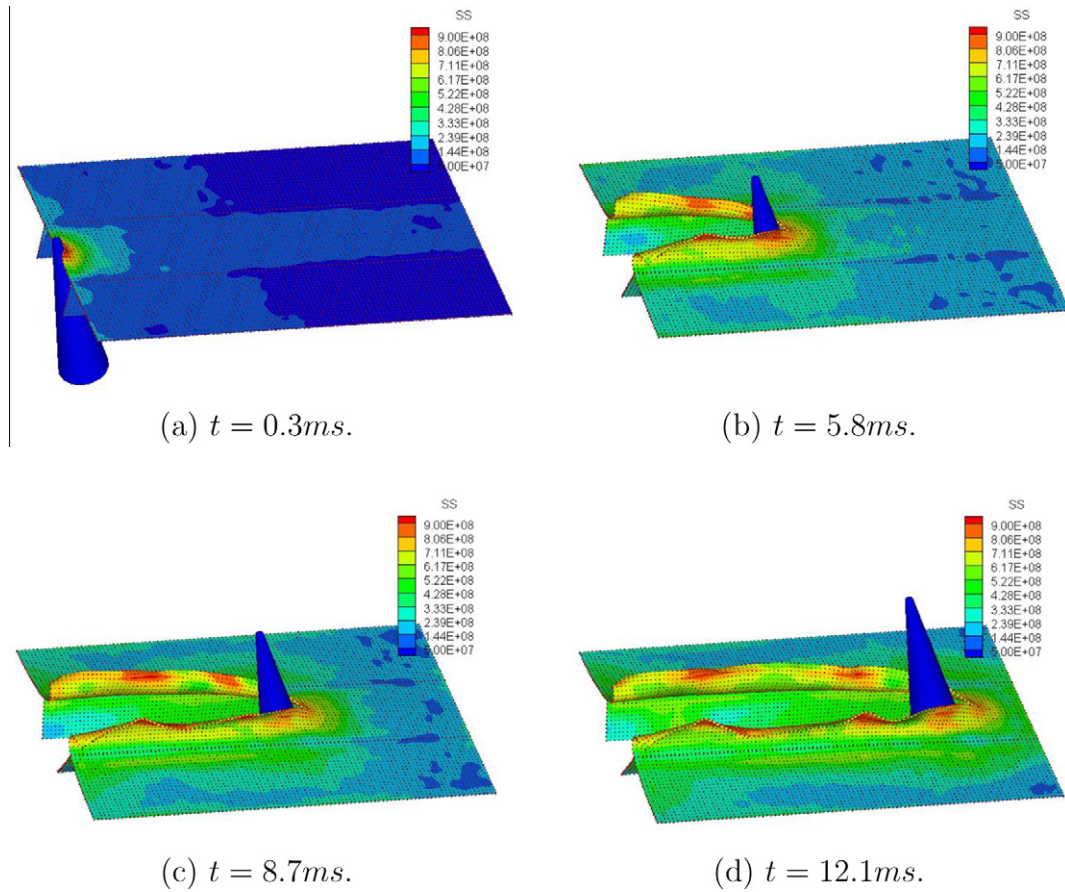


Fig. 14. The fracture history with effective stress as background contour.

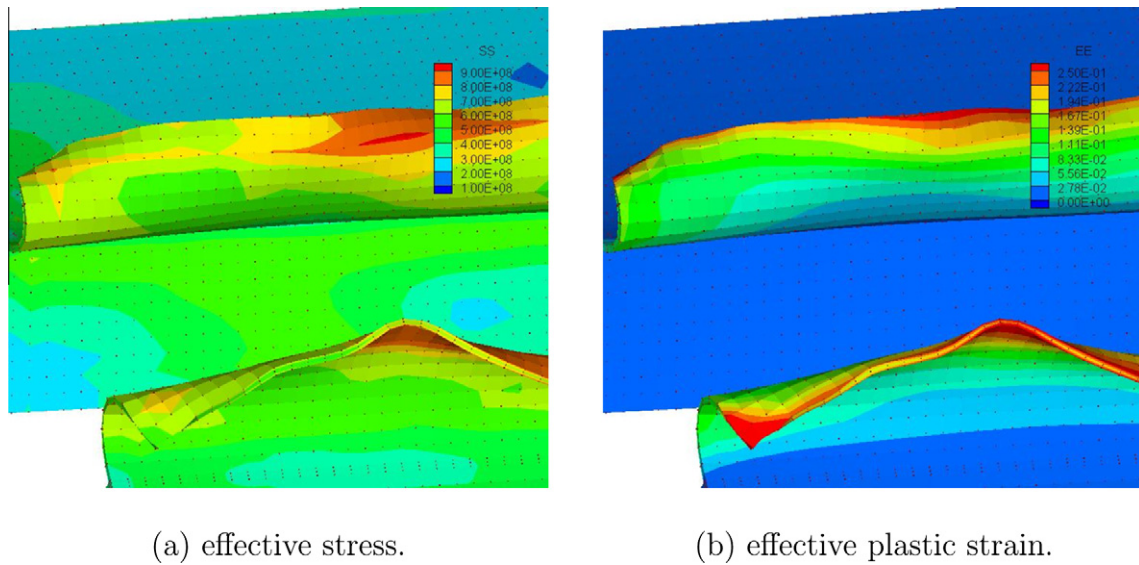


Fig. 15. The detailed deformation morphology nearby crack surface.

25755 nodes and 134400 quadrature points in meshfree simulation, and there are total 3 layers along thickness dimension, i.e., one fiber is composed of three particles. The stiffened plate is Normal Strength steel with material constants listed in Table 1. This paper does not discuss the 3D contact algorithm, which is a 3D extension from the 2D contact algorithm by Ren and Li (2010).

The time sequences of the dynamic fracture process are displayed in Fig. 14 with effective stress as background color contour. From these time sequence plots, one can find that a high stress zone is moving with contact region. With the propagation of crack, the stress at the earlier crack surface is released. This phenomenon illustrates that free boundary condition is automatically formed at

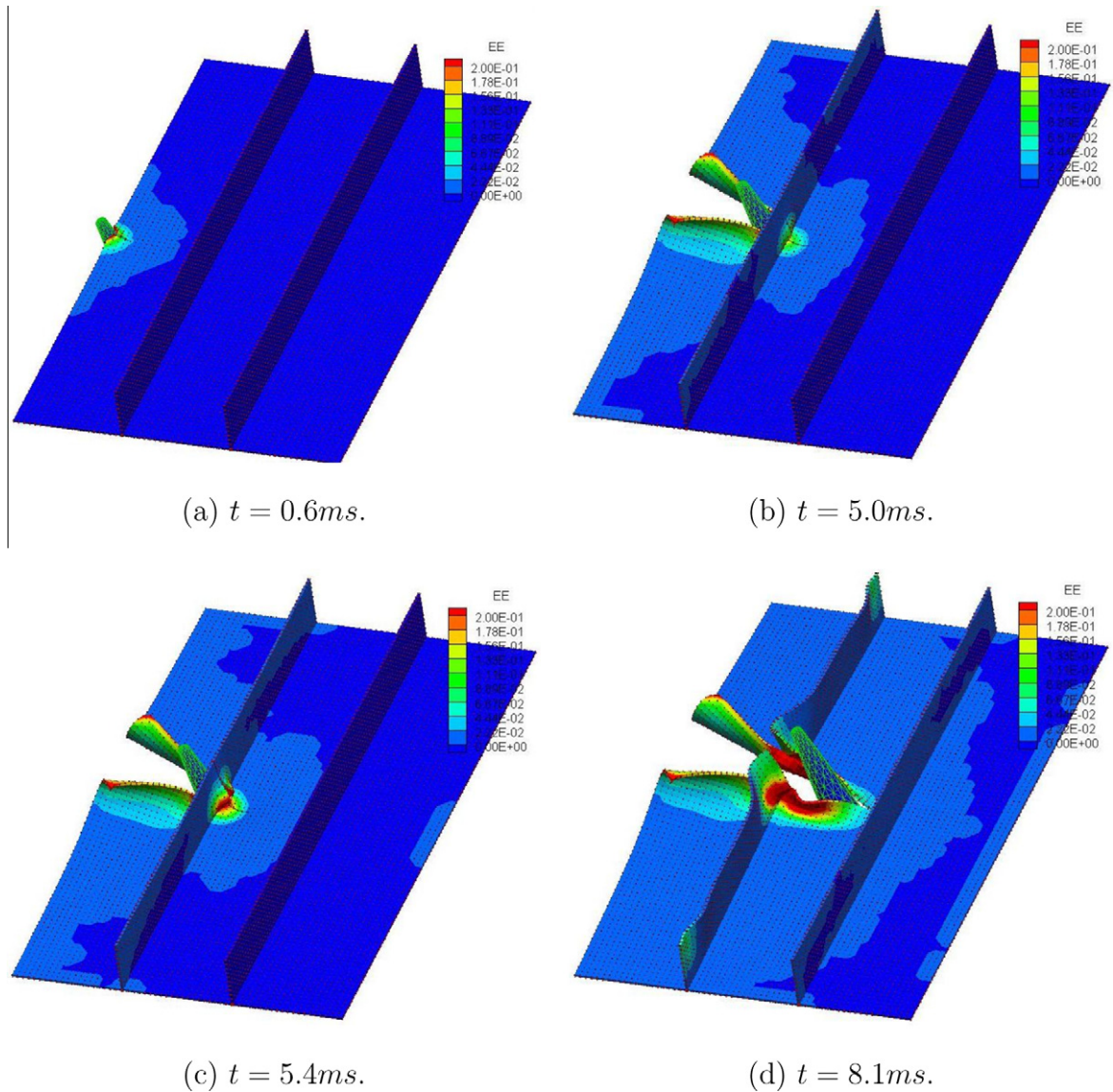


Fig. 16. Fracture history with the effective strain as background contour.

crack surface, which is the crucial point in simulation of crack propagation. And it indicates the perfect performance of proposed 3D crack propagation algorithm. Because of strengthening provided by the flat bar stiffeners under the plate, we can find that most of deformation is limited in a small region. Fig. 15 shows the detailed fracture morphology with effective plastic strain background and one can find dramatic plastic strain distribution in the region between stiffeners, that means most of the impact energy is absorbed inside this region, hence the stiffeners can enhance the strength of the plate structure.

From Fig. 14, one can find high stress spots at crack surface, where the high stress status is not released with time. Zoom in crack surface, the detailed deformation morphology are shown in Fig. 15(b) and (c) with effective stress and effective plastic strain as background color respectively. From Fig. 15, one can find distinct flexural deformation nearby crack surface, the high stress zone is located at where large flexural bending deformation occurs. In the smooth deformed part, the stress is released whereas the effective plastic strain is still high in this region. The flexural deformation phenomenon induced by fracture process, which has been difficult to capture with FEM, has effectively captured by the meshfree simulation.

### 6.3. Simulation II: crack propagation across stiffeners

Simulation I presents numerical results when the crack propagates in the plate area between two stiffeners. However the realistic fracture process normally will go across stiffeners such as ship ground (Simonsen, 1997), which makes crack propagation process more complex. This simulation implements a simulation of crack propagation across stiffeners. The specimen configuration and numerical model are the same as Simulation I, except that the impact loading is imposed at the lateral side as shown in Fig. 13(b). The two edges of the plate that are perpendicular to the impacted edge are prescribed as the fixed displacement boundary. The time sequences of dynamic fracture process are illustrated in Fig. 16 with effective plastic strain contour as background color. With the impact of rigid cone object, the microscopic voids starts to grow, and once the increasing void volume fraction reaches the threshold, crack is set to grow and to propagate as shown in Fig. 16(a). The stiffener can enhance the fracture strength of structure. To observe this, one can find that the deformation of the plate increase significantly when the rigid cone object passes through the stiffener as shown in Fig. 16(b). After the crack cuts through the stiffener, the extra restriction from the stiffener still remains

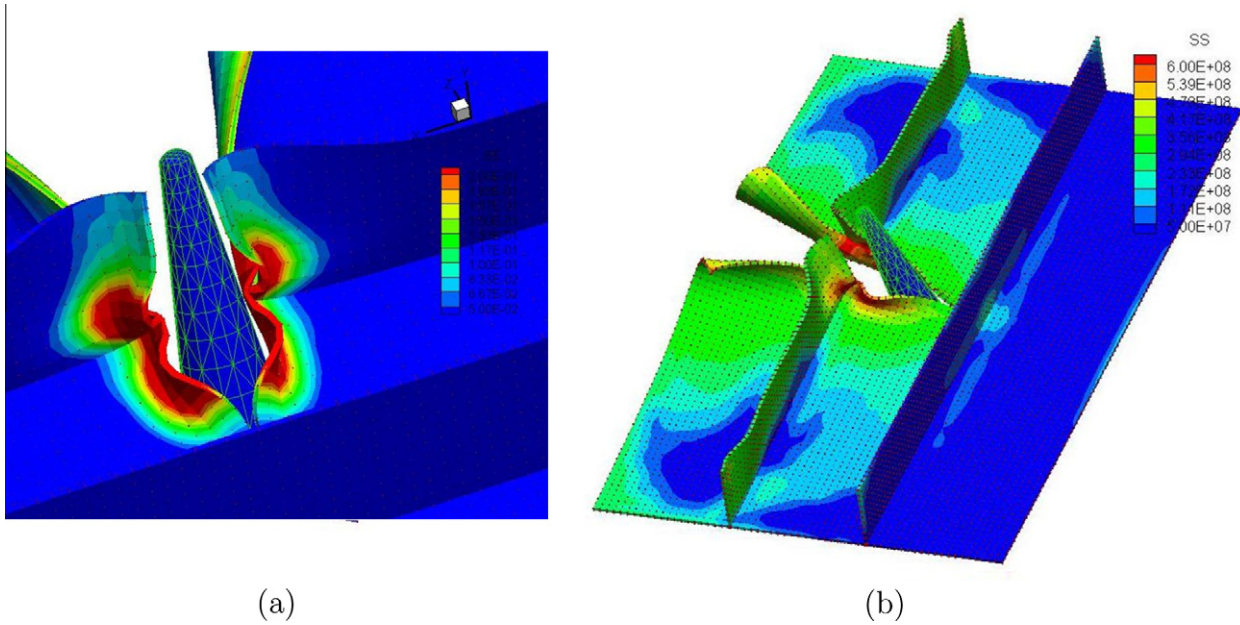


Fig. 17. (a) The detail fracture morphology with background of effective strain, and (b) the fracture morphology with background of effective stress.

against the crack propagation, and one can find that the stiffener and the plate keep deforming while the rigid cone cuts through the structure as shown in Fig. 16(c). When the crack tip is far away from the stiffener, the strengthen enhancement due to stiffener vanishes, and the crack propagates the same way as that in Example I as shown in Fig. 16(d). The detailed damage morphology near a stiffener is shown in Fig. 17(a), where one can find that the plastic strain is very high not only on the stiffener but also on the plate, which means that this zone can absorb large amount of impact energy. The complex flexure deformation pattern has been captured by the meshfree simulation. The impact force on the plate during the cutting motion of the cone is recorded and is shown in Fig. 18, where one can find the stiffener will induce higher contact force when the crack goes through it, and this effect will not disappear immediately until the crack tip is far away from stiffener, it reveals that the stiffener can increase the strength of plate structure significantly. Comparing Fig. 17(b) with (a), one may find that the stress is relaxed along the opening crack surface, which indicates that the 3D visibility condition works, because it does generate a traction-free boundary.

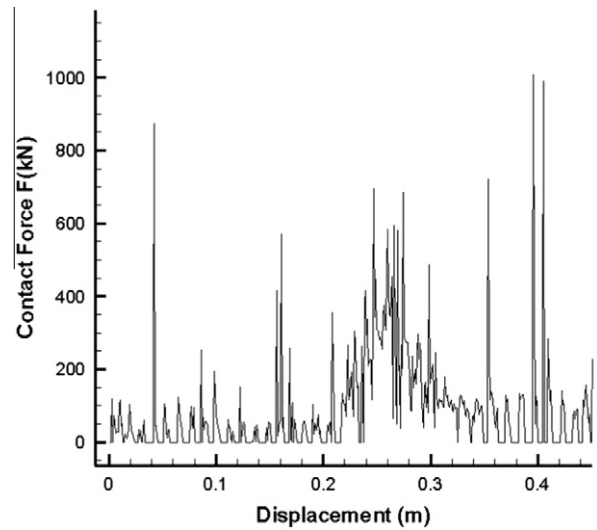


Fig. 18. The contact force history.

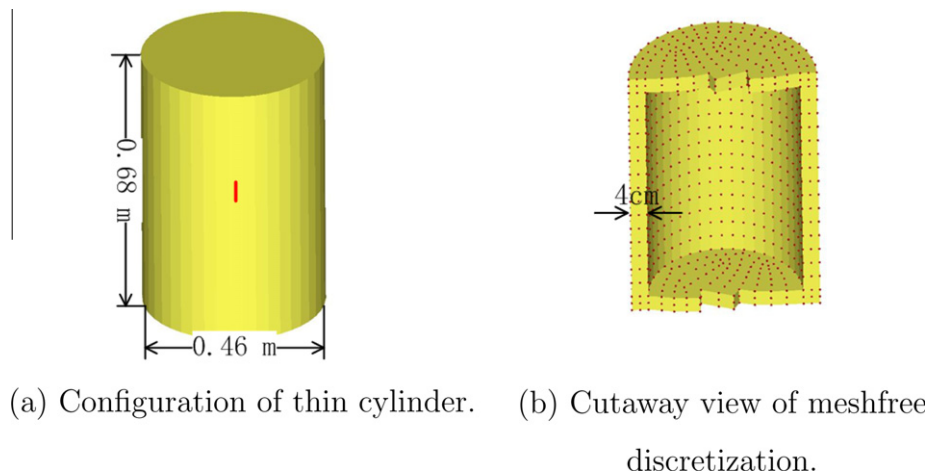


Fig. 19. Pressurized thin cylinder problem.

**Table 2**

Material constants of Johnson-cook model for low alloy steel. \*The parameters of the Johnson-cook damage model is from Borvik et al. (2001) for Weldox 460E steel.

Parameter	Value	Definition
$E$	200 GPa	Young's modulus
$\nu$	0.3	Poisson's ratio
$\rho$	7830 kg m <sup>-3</sup>	mass density
$A$	455 MPa	Yield stress
$B$	237 MPa	Strain hardening
$C$	0.006	
$n$	0.37	Strain hardening index
$\dot{\epsilon}_0$	1000 s <sup>-1</sup>	Reference strain rate
$m$	1.0	Temperature softening
$C_p$	448 J kg <sup>-1</sup> K <sup>-1</sup>	Specific heat
$\alpha$	$11.2 \times 10^{-6}$ K <sup>-1</sup>	Thermal expansion coefficient
$\chi$	0.9	Fraction of plastic work to heat
$\kappa$	38 Wm <sup>-1</sup> K	Thermal conductivity
$T_0$	300 K	Room temperature
$T_m$	1800 K	Melting temperature
$D_1^*$	0.0705	Damage parameter
$D_2$	1.732	Damage parameter
$D_3$	-0.54	Damage parameter
$D_4$	-0.015	Damage parameter
$D_5$	0.0	Damage parameter

The Gurson models adopted in the above simulations are known having mesh-dependency to fracture process. However, the imposed boundary and loading conditions of these examples force the crack path going straight, therefore the simulated crack path result seems to be insensitive to the particle density.

#### 6.4. Simulation III: crack propagation in thin cylinder with Johnson–Cook model

Simulation I and II have demonstrated how to use the proposed method to simulate ductile crack propagation in flat plate structures. In this example, we employ the same methodology to simulate ductile crack propagation in a cylindrical shell structure as shown in Fig. 19, in order to validate the proposed 3D crack growth algorithm for shell structures.

The thin-walled shell structure is a capped cylinder that has 0.68 m in axial length, 0.226 m of mean radius, and a thickness of 0.04 m. In order to initiate fracture, a prescribed crack with length 0.04 m is embedded at the middle cylindrical shell shown as the red line in Fig. 19(a). As described above, the pre-crack is a small slit that is through the thickness of the shell. To drive crack growth, a constant internal pressure ( $3.2 \times 10^8 P_a$ ) is exerted at the inner surface of the cylinder. The whole structure is discretized by uniformly distributed 3468 particles and 18464 Gauss points. As shown in Fig. 19(b), there are three layers of particles along thickness direction of cylinder, i.e., one fiber is composed of three particles in this simulation. The cylinder is made of a low alloy steel modeled by using the Johnson–Cook model. The material constants of the Johnson–Cook model is taken from *Batra and Kim (1992)*, which are listed in Table 2. In the ductile fracture simulation, we set the critical damage value at  $D_c = 0.1$ , at which the macro-crack is set to grow.

The time sequence of this simulation is displayed in Fig. 20 with effective stress contour as the color background. In this simulation, an internal pressure is distributed at the inner surface of the thin cylinder, therefore the cylinder keeps expanding. Fig. 20(a) shows the stress state before the cylinder burst. In Fig. 20(b), the preset crack starts to propagate. Fig. 20(c) and (d) illustrate the crack propagation process. At this time, the separation of crack surface is very small, to show crack path clearly, the crack path is marked with black dots. With the expansion of cylinder, the separation of crack surface increases as shown in

Fig. 20(e) and (f). During this process, the internal pressure maintains a constant value at the inner surface of the cylinder, which may not be realistic; nevertheless we still find stress releasing along crack surface. The Johnson–Cook model is a thermo-mechanical coupling constitutive model, which takes into account the local temperature rise due to the conversion of plastic work into heat. The temperature and effective plastic strain distribution are shown in Fig. 21. One can find that the local temperature increases at the high plastic zone. From Figs. 21 and 20(b), one can find the crack propagates along about a 45° degree angle from the circumference (hoop) direction at the beginning, it is another indication of a shear dominated fracture. One may find that the crack surface shows zig-zag pattern, and this is the main feature of ductile fracture as well. The numerical results shows that the proposed methods can simulate crack propagation in cylindrical surface effectively.

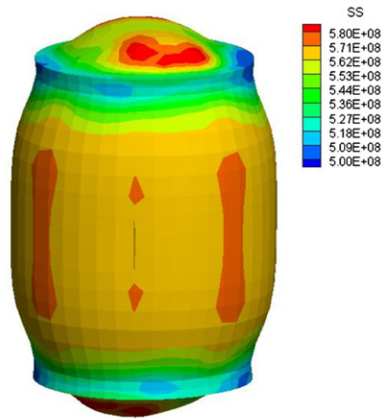
This example is significant in two aspects. First, the Johnson–Cook model is not only rate-dependent but also has thermo-mechanical coupling, and its constitutive parameters will bring the internal length scale into the phenomenological plasticity model. Therefore, mathematically the ductile fracture problem in this example is well-posed, and the same is true in solution of strain localization. For the computational standpoint, the simulation solution of this example is not mesh-dependent, or particle density dependent; as long as one can resolve the intrinsic length scale, the numerical solution will converge to a fixed solution or limit. This is in sharp contrast with the mesh-dependent or mesh-sensitive nature of the various Gurson models discussed in previous sections. Therefore, it is meaningful to demonstrate the capability and the validity of the proposed method to deal with a general well-posed ductile fracture problem.

## 7. Discussions

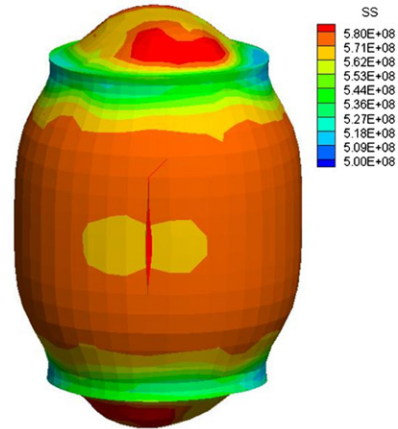
The simulation of ductile fracture in 3D engineering structures is still an ongoing researching subject. In this paper we have presented analytical formulas, constitutive modeling, and computational algorithm to predict crack propagation in large scale plate structures. The numerical results illustrate that the proposed method can successfully simulate crack growth in plate structures undergoing finite deformation and large plastic yielding.

The key technical ingredient in meshfree fracture simulation is how to describe evolving crack surface in computation domain. In this paper, by considering crack propagation in plate structure, we present a detailed crack surface approximation in plate and shell structures, in which the crack surface is represented by an evolving, triangle-piece-wise surface mesh based on the crack growth history. The particle split algorithm is discussed as well, which assures the conservation of mass, momentum and energy during the numerical crack growth. A 3D parametric visibility condition algorithm is proposed to update the meshfree interpolation field. It adjusts the local connectivity map by testing the intersection condition between crack surface triangle facets and line segment between two particles. Any particle line connection that intersects with triangle facet will results the cut-off from the local connectivity map for specified particles. To implement the rate-dependent constitutive law with suitable damage characterization and crack growth criterion is another challenge for 3D ductile fracture simulations. We briefly touched upon the subject by including a simulation example based the rate-dependent Johnson–Cook model.

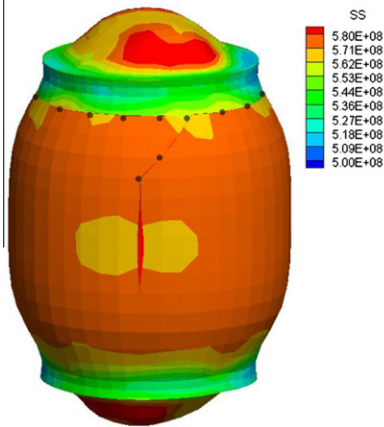
In this work, the constitutive update formulas for finite inelastic deformation with explicit integration are derived for various Gurson models and the Johnson–Cook model. Based on in-plane mode-I fracture experiment, the material parameters for various



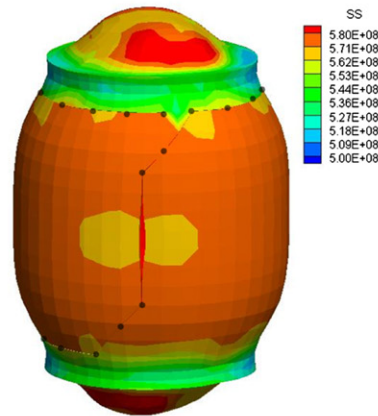
(a)  $t = 9.8ms.$



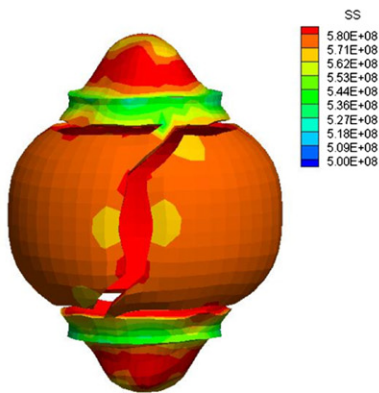
(b)  $t = 11.3ms.$



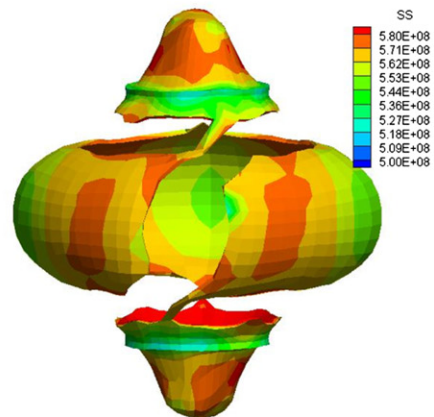
(c)  $t = 11.48ms.$



(d)  $t = 11.51ms.$



(e)  $t = 17.2ms.$



(f)  $t = 23.2ms.$

Gurson-type models are calibrated with experimental data, and their performance are studied and compared. Finally, simulations are carried out to validate the proposed crack growth algorithm for a stiffened plate structures and thin cylindrical shell structures. The results indicate that the proposed method can effectively

predict and capture dynamic fracture process in engineering structures.

Although the numerical simulation has shown that the proposed method works well, there are still many work remained. First, the proposed model uses 3D RKPM meshfree approximation

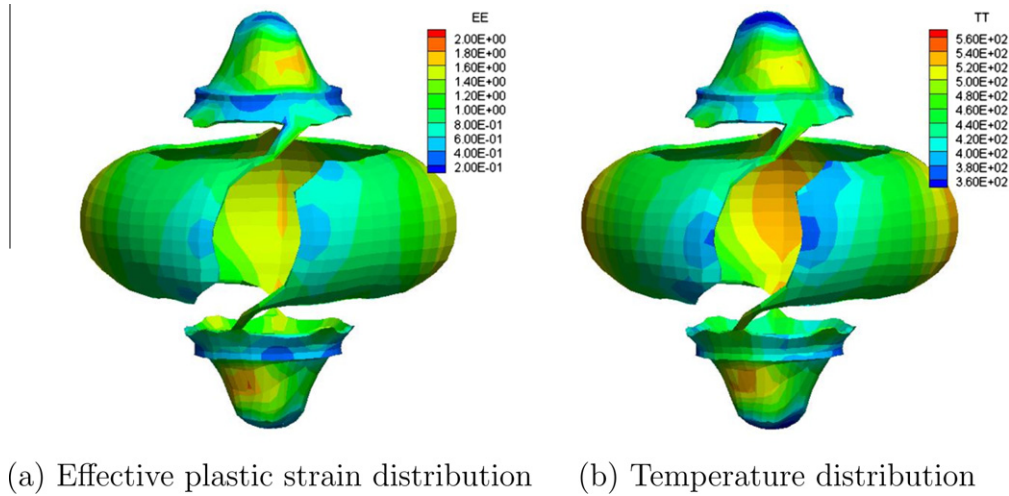


Fig. 21. The effective plastic strain and temperature distribution morphology.

to simulate ductile fracture in shell structures. To make it more efficient and economical in computations, one may need to construct the meshfree shape function for shell structures e.g. [Rabczuk and Areias \(2000\)](#). Second, in this work we only discuss how to grow through thickness cracks. In order to simulate arbitrary three-dimensional crack growth, which is especially important for ductile fracture, we have to develop a general 3D crack surface approximation including a full 3D parametric visibility condition algorithm that can adapt to arbitrary 3D crack surface geometry to simulate arbitrary crack propagation in three-dimensional solids.

**Acknowledgments**

This work is supported by a grant from Office of Navy Research (ONR) to Advanced Dynamic Inc., which sub-contracted to the University of California at Berkeley. We would like to thank the anonymous referees who have made many valuable comments and suggestions to the manuscript of this paper.

**Appendix A. Stress update**

A rate form constitutive equation is used in constitutive update,

$$\dot{\boldsymbol{\sigma}} = \mathbf{C} : \mathbf{d}^e = \mathbf{C} : (\mathbf{d} - \mathbf{d}^p) = \dot{\boldsymbol{\sigma}}^e - \mathbf{C} : \mathbf{d}^p \quad (71)$$

where  $\mathbf{C}$  is material constant tensor:

$$C_{ijkl} = 2G\delta_{ik}\delta_{jl} - (K - 2G/3)\delta_{ij}\delta_{kl} \quad (72)$$

$G$  and  $K$  are engineering shear and bulk modules.

To solve the plastic flow function at time  $t_{n+1}$ , an elastic trial stress is constructed that is accomplished by using the Hughes–Winget formula ([Hughes and Winget, 1980](#)) to take into account the effect of finite rotation,

$$\boldsymbol{\sigma}_{n+1}^e = \mathbf{Q}_{n+1} \boldsymbol{\sigma}_n \mathbf{Q}_{n+1}^T + \Delta t \mathbf{C} : \mathbf{d}_{n+1} \quad (73)$$

$$\mathbf{Q}_{n+1} = \mathbf{I} + (\mathbf{I} - 0.5\mathbf{w}_{n+1})^{-1} \mathbf{w}_{n+1} \quad (74)$$

Cauchy stress tensor  $\boldsymbol{\sigma}$  can be decomposed from the definitions of mean stress and effective stress:

$$\boldsymbol{\sigma} = \sigma_m \mathbf{I} + \frac{2}{3} \sigma_e \hat{\mathbf{n}} \quad (75)$$

where

$$\hat{\mathbf{n}} = \frac{3}{2\sigma_e} \mathbf{s} \quad (76)$$

The plastic flow rule gives,

$$\mathbf{d}^p = \dot{\lambda} \frac{\partial \Phi}{\partial \boldsymbol{\sigma}} = \dot{\lambda} \left\{ \frac{1}{3} \frac{\partial \Phi}{\partial \sigma_m} \mathbf{I} + \frac{\partial \Phi}{\partial \sigma_e} \hat{\mathbf{n}} \right\} \quad (77)$$

Define:

$$D_m = \dot{\lambda} \frac{\partial \Phi}{\partial \sigma_m} \quad (78)$$

$$D_e = \dot{\lambda} \frac{\partial \Phi}{\partial \sigma_e} \quad (79)$$

The plastic part rate of deformation can be decomposed as:

$$\mathbf{d}^p = \frac{1}{3} D_m \mathbf{I} + D_e \hat{\mathbf{n}} \quad (80)$$

Substituting Eq. (80) back into Eq. (74), the stress relaxation from the trial stress is given by:

$$\boldsymbol{\sigma}_{n+1} = \boldsymbol{\sigma}_{n+1}^e - K \Delta t D_m \mathbf{I} - 2G \Delta t D_e \hat{\mathbf{n}}_{n+1} \quad (81)$$

The mean and effective components of Eq. (75) are:

$$\sigma_m = \sigma_m^e - \Delta t K D_m \quad (82)$$

$$\sigma_e = \sigma_e^e - \Delta t K D_e \quad (83)$$

The time integration schedule assume constant  $D_m$  and  $D_e$  during a time step, which is consistent with the global, explicit integration method.

Eq. (81) shows that the relaxation in the deviatoric stress space is along  $\hat{\mathbf{n}}_{n+1}$ , which can be determined from the trial stress tensor:

$$\hat{\mathbf{n}}_{n+1} = \frac{3}{2\sigma_e^e} \mathbf{s}^e \quad (84)$$

where  $\sigma_e^e$  and  $\mathbf{s}^e$  are effective stress, and deviatoric stress from  $\boldsymbol{\sigma}_{n+1}^e$ . Thereby the stress update Eq. (81) is determined by two unknown variables  $D_m$  and  $D_e$ .

The plastic flow, Eq. (43), are governed by the microscopic yield stress  $\sigma_M$  of the matrix material. The matrix material properties include Young’s modulus  $E$ , its initial yield stress is  $\sigma_M^0$ , and material hardening law  $\dot{e}_M^p(\sigma_M)$ .

The condition that macroscopic plastic work equates to the energy dissipated in the matrix material during plastic deformation may be expressed as follows,

$$(1 - f) \sigma_M \dot{e}_M^p = \boldsymbol{\sigma} : \mathbf{d}^p \quad (85)$$

From the above equation, we can obtain the plastic strain rate in matrix material,

$$\dot{\epsilon}_M^p = \frac{\boldsymbol{\sigma} : \mathbf{d}^p}{(1-f)\sigma_M} = \frac{\sigma_m D_m + 1.5\sigma_e D_e}{(1-f)\sigma_M} \quad (86)$$

The plastic flow function shows that the two internal variables  $\epsilon_M^p$  and  $f$  determine the damage state of the material. Based on Eqs. (44), (46), (51) and (86), the time integration of plastic strain can be found as,

$$\epsilon_{M,n+1}^p = \epsilon_{M,n}^p + \Delta t \dot{\epsilon}_M^p \quad (87)$$

$$f_{n+1} = f_n + \Delta t \dot{f} \quad (88)$$

The definitions of  $\dot{\epsilon}_M^p$  and  $\dot{f}$  show that they are related to two unknown variables:  $D_m$  and  $D_e$  as well as the stress update in Eq. (81).

In this work, we use the central difference method in explicit time integration. Given stress state  $\sigma_n$  at time step  $n$ , denote the time step as  $\Delta t$ , the rate of deformation  $D$  can be calculated by using Eq. (4). To determine the stress state  $\sigma_{n+1}$  at time step  $n + 1$ , Eq. (81) indicates that the two unknown  $D_m$  and  $D_e$  must be solved simultaneously.

Here  $D_m$  and  $D_e$  must satisfy the self-relation in Eqs. (78) and (79), and the plastic flow function Eq. (43):

$$f_1(D_m, D_e) = D_m \frac{\partial \Phi}{\partial \sigma_e} + D_e \frac{\partial \Phi}{\partial \sigma_m} = 0 \quad (89)$$

$$f_1(D_m, D_e) = \Phi(D_m, D_e) = 0 \quad (90)$$

To solve above equations, an iterative Newton method is used, the roots ( $D_m$  and  $D_e$ ) are determined in a predict-correct iteration by improving the initial, predicted estimate ( $D_m^k$  and  $D_e^k$ ):

$$D_m^{k+1} = D_m^k + \Delta D_m^k \quad (91)$$

$$D_e^{k+1} = D_e^k + \Delta D_e^k \quad (92)$$

where  $k$  is iterative counter. The correction ( $\Delta D_m^k, \Delta D_e^k$ ) is calculated by solving the following equations of the first-order Taylor expansion of  $f_1$  and  $f_2$ ,

$$f_1^{k+1} = f_1^k + \frac{\partial f_1^k}{\partial D_m} \Delta D_m^k + \frac{\partial f_1^k}{\partial D_e} \Delta D_e^k = 0 \quad (93)$$

$$f_2^{k+1} = f_2^k + \frac{\partial f_2^k}{\partial D_m} \Delta D_m^k + \frac{\partial f_2^k}{\partial D_e} \Delta D_e^k = 0 \quad (94)$$

### Appendix B. Derivatives of damage parameters

For the plastic-damage flow rule, the original Gurson model has,

$$\frac{\partial f^*(f)}{\partial f} = 1 \quad (95)$$

whereas for other Gurson models have,

$$\frac{\partial f^*(f)}{\partial f} = \begin{cases} 1 & f \leq f_c \\ \frac{1/q_1 - f_c}{f_f - f_c} & f > f_c \end{cases} \quad (96)$$

To be consistent with the expression in Simonsen and Li (2004) (Appendices A and B), we first define the following notations,

$$\begin{aligned} H_1 &= \epsilon_M^p \\ H_2 &= f \\ h_1 &= \dot{\epsilon}_M^p \\ h_2 &= \dot{f} \end{aligned} \quad (97)$$

Different Gurson models use different formulas to calculate  $\dot{f}$ , consequently the derivations of  $h_2$  are different as well.

For the original Gurson model, GTN model and SM-Gurson model, the derivatives of  $h_2$  are:

$$\begin{aligned} \frac{\partial h_2}{\partial H_1} &= A_N \left[ \frac{\partial h_1}{\partial H_1} - \frac{(H_1 - \epsilon_N)h_1}{s_N^2} \right] & \frac{\partial h_2}{\partial H_2} &= \widetilde{-D_m} + A_N \frac{\partial h_1}{\partial H_2} + \overline{k_w \omega D_e} \\ \frac{\partial h_2}{\partial \sigma_m} &= A_N \frac{\partial h_1}{\partial \sigma_m} & \frac{\partial h_2}{\partial \sigma_e} &= A_N \frac{\partial h_1}{\partial \sigma_e} \\ \frac{\partial h_2}{\partial D_m} &= \widetilde{1-f} + A_N \frac{\partial h_1}{\partial D_m} & \frac{\partial h_2}{\partial D_e} &= A_N \frac{\partial h_1}{\partial D_e} + \overline{k_w f \omega} \end{aligned} \quad (98)$$

Here on the left side of Eq. (98), the terms with over script  $\widetilde{\phantom{x}}$  indicate that these terms are present in the original Gurson model, GTN model and SM-Gurson model; similarly, the terms with over-script  $\overline{\phantom{x}}$  means that these terms are present in GTN model and SM-Gurson model, and the terms with overline only present in SM-Gurson model. For example, there is no term associated with the original Gurson model for the derivatives,  $\frac{\partial h_2}{\partial H_1}$ ,  $\frac{\partial h_2}{\partial \sigma_m}$ ,  $\frac{\partial h_2}{\partial \sigma_e}$  and  $\frac{\partial h_2}{\partial D_e}$ , these derivative of  $h_2$  equals zero for original Gurson model.

For the M-Gurson model,  $\dot{f}_s$  is given in Eq. (52), and the derivatives of  $h_2$  are given as follows,

$$\begin{aligned} \frac{\partial h_2}{\partial H_1} &= A_N \left[ \frac{\partial h_1}{\partial H_1} - \frac{(H_1 - \epsilon_N)h_1}{s_N^2} \right], & \frac{\partial h_2}{\partial H_2} &= -D_m + A_N \frac{\partial h_1}{\partial H_2} + k_w \Omega(T) \omega_0 D_e \\ \frac{\partial h_2}{\partial \sigma_m} &= \begin{cases} A_N \frac{\partial h_1}{\partial \sigma_m} & T < T_1 \\ A_N \frac{\partial h_1}{\partial \sigma_m} + \frac{1}{\sigma_e(T_1 - T_2)} k_w f \omega_0 D_e & T_1 \leq T \leq T_2 \\ A_N \frac{\partial h_1}{\partial \sigma_m} & T > T_2 \end{cases} \\ \frac{\partial h_2}{\partial \sigma_e} &= \begin{cases} A_N \frac{\partial h_1}{\partial \sigma_e} & T < T_1 \\ A_N \frac{\partial h_1}{\partial \sigma_e} + \frac{\sigma_m}{\sigma_e^2(T_1 - T_2)} k_w f \omega_0 D_e & T_1 \leq T \leq T_2 \\ A_N \frac{\partial h_1}{\partial \sigma_e} & T > T_2 \end{cases} \\ \frac{\partial h_2}{\partial D_m} &= 1 - f + A_N \frac{\partial h_1}{\partial D_m} & \frac{\partial h_2}{\partial D_e} &= A_N \frac{\partial h_1}{\partial D_e} + k_w f \Omega(T) \omega_0 \end{aligned} \quad (99)$$

The other variable derivatives in Eq. (52) can be found in Simonsen and Li (2004).

### References

Alsos, H.S., Amdahl, J., 2009. On the resistance to penetration of stiffened plates. Part I: Experiments. *International Journal of Impact Engineering* 36, 799–807.

Alsos, H.S., Amdahl, J., Hopperstad, O.S., 2009. On the resistance to penetration of stiffened plates. Part II: Numerical analysis. *International Journal of Impact Engineering* 36, 875–887.

Anderson, T.L., 1995. *Fracture Mechanics-Fundamentals and Applications*, 2nd ed. CRC Press, Boca Raton, FL.

Antoun, T., Seaman, L., Curran, D.R., Kane, G.I., Razorenov, S.V., Utkin, A.V., 2003. *Spall Fracture*. Springer, New York.

Aravas, N., 1987. On the numerical integration of a class of pressure-dependent plasticity models. *International Journal for Numerical Methods in Engineering* 24, 1395–1416.

Batra, R.C., Kim, C.H., 1992. Analysis of shear banding in twelve materials. *International Journal of Plasticity* 8, 425–452.

Belytschko, T., Lu, Y.Y., Gu, L., 1995. Crack propagation by element-free Galerkin methods. *Engineering Fracture Mechanics* 51, 295–315.

Bordas, S., Rabczuk, T., Zi, G., 2008. Three-dimensional crack initiation, propagation, branching and junction in non-linear materials by an extended meshfree method without asymptotic enrichment. *Engineering Fracture* 28, 943–960.

Borvik, T., Hopperstad, O.S., Berstad, T., Langseth, M., 2001. Numerical simulation of plugging failure in ballistic penetration. *International Journal of Solids and Structures* 38, 6241–6264.

Chen, E.P., 1992. Numerical simulation of shear induced plugging in HY100 steel plates. *International Journal of Damage Mechanics* 1, 32–43.

Chevrier, P., Klepaczko, J.R., 1999. Spall fracture: mechanical and microstructural aspects. *Engineering Fracture Mechanics* 63, 273–294.

Chu, C.C., Needleman, A., 1980. Void nucleation effects in biaxially stretched sheets. *Journal of Engineering Materials and Technology* 102, 249–256.

- Cirak, F., Ortiz, M., Pandolfi, A., 2005. A cohesive approach to thin-shell fracture and fragmentation. *Computer Methods in Applied Mechanics and Engineering* 194, 2604–2618.
- Erdogan, F., Ratwani, M., 1972. Fracture of cylindrical and spherical shells containing a crack. *Nuclear Engineering and Design* 20, 265–286.
- Gurson, A.L., 1977. Continuum theory of ductile rupture by void nucleation and growth – Part I. Yield criteria and flow rules for porous ductile media. *Journal of Engineering Materials and Technology* 2, 2–15.
- Hughes, T.J.R., Winget, J., 1980. Finite rotation effects in numerical integration of rate constitutive equations arising in large-deformation analysis. *International Journal for Numerical Methods in Engineering* 15, 1862–1867.
- Johnson, G.R., Cook, W.H., 1983. A constitutive model and data for metals subjected to 1176 large strains, high strain rates and high temperature. In: *Proceedings of the 1177 Seventh International Symposium on Ballistics*, pp. 1–7.
- Johnson, G.R., Cook, W.H., 1985. Fracture characteristics of three metals subjected to 1179 various strains, strain rates, temperatures and pressures. *Engineering Fracture* 21, 31–48.
- Li, S., Liu, W.K., 2004. *Meshfree Particle Method*. Springer-Verlag, Berlin, Germany.
- Li, S., Simonsen, B.C., 2005. Meshfree simulations of ductile crack propagation. *International Journal of Computational Engineering Science* 6, 1–25.
- Liu, W.K., Hao, S., Belytschko, T., Li, S., Chang, C.T., 1999. Multiple scale meshfree methods for damage fracture and localization. *Computational Materials Science* 16, 197–205.
- Lucy, L.B., 1977. A numerical approach to the testing of the fission hypothesis. *Astrophysical Journal* 82, 1013–1024.
- Mathur, K.K., Needleman, A., Tvergaard, V., 1996. Three dimensional analysis of dynamic ductile crack growth in a thin plate. *Journal of the Mechanics and Physics of Solids* 44, 439–459.
- Mikkelsen, L.P., 1997. Post-necking behaviour modelled by a gradient dependent plasticity theory. *International Journal of Solids and Structures* 34, 4532–4546.
- Nahshon, K., Hutchinson, J.W., 2008. Modification of the Gurson Model for shear failure. *European Journal of Mechanics A/Solids* 27, 1–17.
- Nielsen, K., Tvergaard, V., 2009. Effect of a shear modified Gurson model on damage development in a FSW tensile specimen. *International Journal of Solids and Structures* 46, 587–601.
- Nielsen, K., Tvergaard, V., 2010. Ductile shear failure or plug failure of spot welds modelled by modified Gurson model. *Engineering Fracture Mechanics* 77, 1031–1047.
- Nahshon, K., Xue, Z., 2009. A modified Gurson model and its application to punch-out experiments. *Engineering Fracture Mechanics* 76, 997–1009.
- Moës, N., Dolbow, J., Belytschko, T., 1999. A finite element method for crack growth without remeshing. *International Journal for Numerical Methods in Engineering* 46, 133–150.
- Qian, D., Eason, T., Li, S., Liu, W.K., 2008. Meshfree simulation of failure modes in thin cylinder subjected to combined loads of internal pressure and localized heat. *International Journal for Numerical Methods in Engineering* 76, 1159–1180.
- Rabczuk, T., Areias, P., 2000. A meshfree thin shell for arbitrary evolving cracks based on an extrinsic basis. *CMES* 1, 11–26.
- Rabczuk, T., Zi, G., 2007. A meshfree method based on the local partition of unity for cohesive cracks. *Computational Mechanics* 39, 743–760.
- Rabczuk, T., Bordas, S., Zi, G., 2007. A three-dimensional meshfree method for continuous multiple-crack initiation, propagation and junction in statics and dynamics. *Computational Mechanics* 40, 473–495.
- Rabczuk, T., Zi, G., Bordas, S., Nguyen-Xuan, H., 2008. A geometrically non-linear three-dimensional cohesive crack method for reinforced concrete structures. *Engineering Fracture Mechanics* 75, 4740–4758.
- Ren, B., Li, S., 2010. Meshfree simulations of plugging failures in high-speed impacts. *Computers and Structures* 88, 909–923.
- Ren, B., Li, S., Qian, J., Zeng, X., 2011a. Meshfree simulations of spall fracture. *Computer Methods in Applied Mechanics and Engineering* 200, 797–811.
- Ren, B., Qian, J., Zeng, X., Jha, A.K., Xiao, S., Li, S., 2011b. Recent developments on thermo-mechanical simulations of ductile failure by meshfree method. *Computer Modeling in Engineering and Sciences* 71, 253–277.
- Rice, J.R., Tracey, D.M., 1969. On the ductile enlargement of voids in triaxial stress fields. *Journal of the Mechanics and Physics of Solids* 17, 201–217.
- Song, J.H., Belytschko, T., 2009. Dynamic fracture of shells subjected to impulsive loads. *ASME Journal of Applied Mechanics* 76. Article No. 051301.
- Simkins, D.C., Li, S., 2006. Meshfree simulations of thermo-mechanical ductile fracture. *Computational Mechanics* 38, 235–249.
- Simonsen, C.B., 1997. *Ship Grounding on Rock II: Validation and Application*. *Marine Structures* 10, 563–584.
- Simonsen, C.B., Tornqvist, R., 2004. Experimental and numerical modeling of ductile crack propagation in large-scale shell structures. *Marine Structures* 17, 1–27.
- Simonsen, C.B., Li, S., 2004. Mesh-free simulation of ductile fracture. *International Journal for Numerical Methods in Engineering* 60, 1425–1450.
- Tvergaard, V., Needleman, A., 1984. Analysis of the cup-cone fracture in a round tensile bar. *Acta Metallurgica* 32, 157–169.
- Tvergaard, V., Hutchinson, J.W., 1996. Effect of strain-dependent cohesive zone model on predictions of crack growth resistance. *International Journal of Solids and Structures* 33, 3297–3308.
- Tvergaard, V., 2001. Crack growth predictions by cohesive zone model for ductile fracture. *Journal of the Mechanics and Physics of Solids* 49, 2191–2207.